Flow and bathymetry in sharp open-channel bends: Experiments and predictions

Jie Zeng,[1] George Constantinescu,[2] Koen Blanckaert,[3,4] and Larry Weber[2]

[1]   This paper focuses on experiments and simulations conducted in very sharp open-channel bends with flat and equilibrium bathymetry, corresponding to the initial and final phases of the erosion and deposition processes, respectively. The study of flow in curved open bends is relevant for flow in natural river configurations, as most river reaches are not straight. The configuration considered in the present work was designed as a test case in which the role of the cross-sectional flow is more severe than in meandering natural river reaches (radius of curvature of the channel is close to the channel width) and, thus, can serve for validation of numerical models used to predict flow and sediment transport in river engineering applications. This paper presents detailed new experimental data on the equilibrium bathymetry as well as depth-averaged distributions, vertical profiles, and cross-sectional patterns of the streamwise velocity, the cross-stream circulation, streamwise vorticity, and the turbulent kinetic energy at the initial and final stages of the erosion and deposition processes. The numerical simulations are performed using a three-dimensional nonhydrostatic RANS model for flow, sediment transport, and bathymetry, which employs fine meshes, accounts for the effect of small bed forms, and avoids the use of the law of the wall. The model predicts, rather accurately, the distribution of the streamwise velocity, the cross-stream circulation, and the turbulent kinetic energy in the simulations conducted with a fixed (flat and deformed bed corresponding to equilibrium conditions) prescribed bathymetry. In the case of a simulation conducted with loose bed, the model predicts satisfactorily the main features of the bathymetry at equilibrium conditions, despite the fact that including the interaction between the flow and the bathymetry increases the overall uncertainty in the model predictions. Results indicate that both improvements in the level of turbulence modeling and in the modeling of the sediment transport would allow further improvement in the predictive capabilities of morphodynamic models.

1.   Introduction

[2]   Processes in natural river configurations are characterized by an important interaction between the 3D flow field, the sediment transport and the bathymetry. Cross-stream motion, for example, is of particular importance since it redistributes the velocity, influences the direction and magnitude of the boundary shear stress and the sediment transport, affects the bathymetry evolution, and the spreading and mixing of suspended matter like contaminants or nutrients.

[3]   Prediction and knowledge of the 3D flow, sediment transport and bathymetry are important in river engineering and management, for example in the design of river revitalization projects, the maintenance and optimization of navigation fairways, the improvement of ecological river functions, etc.

[4]   Two-dimensional (2D) depth-averaged models are presently the most commonly used tools to predict flow, sediment transport and bathymetry in rivers. Models have been proposed by, e.g., *Shimizu and Itakura* [1989], *Kassem and Chaudhry* [2002], *Darby et al.* [2002], *Minh Duc et al.* [2004], *Wu* [2004], and *Choi et al.* [2005]. The major shortcoming of these models is that they cannot account for the vertical structure of the flow field, and especially for cross-stream circulation that is a predominant mechanism in complex 3D river configurations [*Rozovskii*, 1957; *Blanckaert*, 2001; *Blanckaert and Graf*, 2004]. Semi-empirical submodels for curvature induced cross-stream circulation (also called secondary flow, spiral flow or helical flow) have been developed and implemented by, e.g., *Struiksma et al.* [1985], *Finnie et al.* [1999], *Kassem and Chaudhry* [2002], *Blanckaert and de Vriend* [2003], and *Blanckaert et al.* [2003]. Parameterization of the vertical flow structure can also be obtained by appending moment-of-momentum equa-

[1]Operation and Hydro Data Management Division, South Florida Water Management District, West Palm Beach, Florida, USA.
[2]Department of Civil and Environmental Engineering, IIHR-Hydroscience and Engineering, University of Iowa, Iowa City, Iowa, USA.
[3]Faculty of Civil Engineering and Geosciences, Delft University of Technology, Delft, Netherlands.
[4]ICARE-ENAC, Ecole Polytechnique Fédérale, Lausanne, Switzerland.

tions to the original 2D model [e.g., see *Yeh and Kennedy*, 1993; *Jin and Steffler*, 1993; *Ghamry*, 1999; *Ghamry and Steffler*, 2005; *Vasquez et al.*, 2005]. These so-called quasi-3D models only yield satisfactory results in relatively simple river configurations, such as weakly to moderately curved open-channel bends.

[5] Three-dimensional computations of the flow in curved open-channel bends have been published starting in the late 1970s (e.g., see discussion by *Celik and Rodi* [1988]). Fully three-dimensional (3D) nonhydrostatic models of flow and sediment transport in loose bed channels have recently become computationally feasible. Such models have been successfully applied to the case of moderately (ratio between the mean curvature and channel width was larger than four) curved open-channel bends by *Shimizu et al.* [1990], *Wu et al.* [2000], *Ruther and Olsen* [2005, 2006], and *Zeng et al.* [2005a, 2005b, 2008] and by *Khosronejad et al.* [2007].

[6] Whether or not these 3D models can accurately predict fluvial processes in the more complex natural river environment is not entirely clear. This is partly because our understanding of the relevant processes are mainly based on knowledge acquired in simplified laboratory configurations. Progress is hampered by the lack of detailed experimental data in complex 3D flow configurations that would allow enhancing the insight in the relevant processes and validating numerical tools.

[7] The development of generic insight and reliable engineering and management tools for the natural river environment is complicated by the wide variety of encountered bathymetries and configurations. This paper focuses on a sharp single open-channel bend configuration which was designed to include all processes occurring in the natural river environment in an exaggerated way, in order to make them better visible and to allow validation of a 3D morphodynamic model by means of an extremely severe test case (e.g., in terms of the strength and importance of cross-stream motions).

[8] This paper:

[9] Provides experimental data on the 3D distributions of the mean flow velocity and turbulence measured with high spatial and temporal resolution in two experiments in a sharp open-channel bend; the first over a flat bed and the second over an equilibrium mobile bed bathymetry under similar hydraulic conditions. The experiments are representative for the initial and the final configuration of the scour and deposition process in strongly-curved open-channel bends, respectively. The ratio between the mean curvature, R, and the channel width, B, in the present experiments is close to 1.3 which is much lower than the values considered in previous experimental investigations [e.g., *Blanckaert*, 2001; *Blanckaert and Graf*, 2004; *Blanckaert et al.*, 2003; *Blanckaert and de Vriend*, 2003, 2005a, 2005b] for which the ratio was larger than 4. Consequently, the strength of the cross-stream motions is more important and this case is tougher to predict by numerical simulations.

[10] Validates and evaluates the hydrodynamic and morphodynamic modules of a nonhydrostatic 3D Reynolds Averaged Navier-Stokes solver for flow, sediment transport and bathymetry by means of the presented experimental data for strongly curved bends. The hydrodynamic module avoids the use of the law of the wall and applies meshes

sufficiently fine to integrate the governing equations through the viscous sublayer. This model has already been validated for straight river configurations and moderately curved open-channel bend configurations [*Zeng et al.*, 2005a, 2008]. To the best of our knowledge this is the first time a fully 3D RANS model with movable bed capabilities was used to predict the flow and equilibrium bathymetry in such a complex channel bend configuration (ratio $R/B = 1.3$). These flow conditions are very challenging for 3D RANS models and, in particular, for the ones with movable bed capabilities.

[11] Uses the experimental and numerical simulation data to enhance insight in the physics of the flow in bends of very strong curvature over flat and equilibrium bathymetry. For example, the numerical simulations allow to predict the bed shear stress distribution over the entire bed and to estimate the distribution of a Chezy type coefficient which has to be prescribed in depth-averaged 2D flow models that are widely used in river engineering.

[12] Allows estimating how much of the differences between the simulation results and experimental measurements are due to the turbulence model and how much they are due to errors in predicting the bathymetry profiles. This is done by comparing results from experiment with results from a simulation with fixed deformed bed (equilibrium bathymetry obtained from experiment) and from a simulation with movable bed in which the equilibrium bathymetry is predicted by the model. The differences between experiment and the fixed deformed bed simulation are due mainly to the turbulence model used. The differences between the experiment and the movable bed simulation are due to both the turbulence model and the sediment transport model.

2. The Experiments

[13] Figure 1 shows the flume at EPFL in which two series of experiments were carried out [*Blanckaert*, 2002]: the *H89* experiment with a flat bed and the *M89* experiment with a mobile bed. The flume consisted of three sections: a 9-m-long straight inflow channel reach followed by a 193° bend with constant centerline radius of curvature $R = 1.7$ m and a 5-m-long straight outflow reach. The total length of the flume was 22.7 m along the centerline. The width of the flume was $B = 1.3$ m and lateral walls (banks) were vertical. The bed was covered with quasi-uniform sand having diameters in the range 1.6 mm–2.2 mm with an average of about $d_{50} = 2$ mm.

[14] The *H89* experiment was carried out with a flat sand bed, which was immobilized by means of a paint sprayed on it, thereby not modifying the sand roughness. The channel slope was 0.22 % in the straight inflow reach, and the bed was horizontal in the rest of the flume.

[15] The *M89* mobile bed experiments started from an identical initial configuration but with loose bed. Sediment was fed at a constant rate of $q_s = 0.023$ kgm^{-1} s^{-1} at the flume's entrance. Sediment felled from a funnel on a plate, and moved into the flume by means of a back-and-forth moving scraper. Only bed-load sediment transport occurred, with no suspended sediment transport. Once a state of dynamic equilibrium was reached, characterized by small migrating dunes superimposed on the steady macro features of the bathymetry, sediment supply was stopped and the bathymetry was frozen by spraying paint on it.
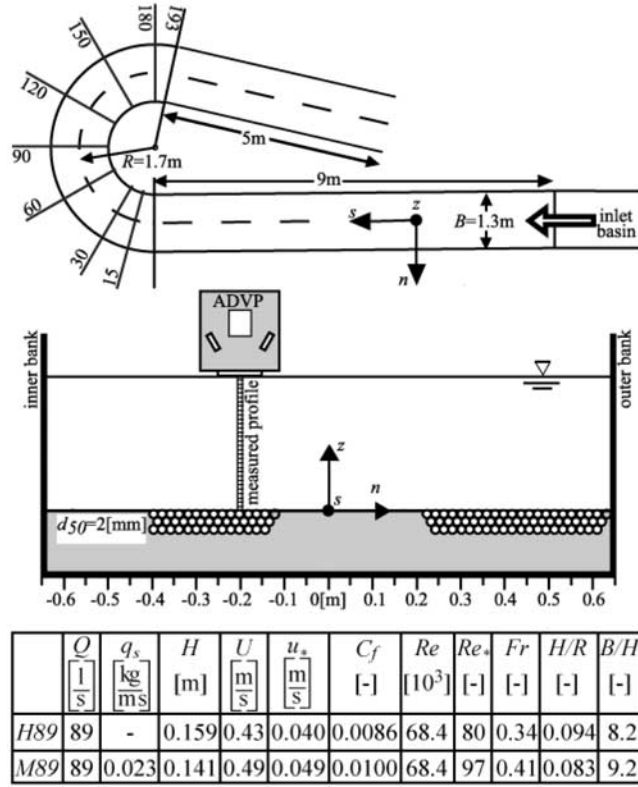
Figure 1. Experimental setup, reference system, ADVP, and hydraulic conditions. Q, discharge; q_s, unit sediment discharge; H, flume-averaged flow depth; $U = Q/(BH)$, flume-averaged velocity; u_*, flume-averaged shear velocity; $C_f = (u_*/U)^2$, Chézy type friction factor; $Re = UH/\nu$, Reynolds number; $Re_* = u_* d_{50}/\nu$, particle Reynolds number; $Fr = U/\sqrt{gH}$, Froude number.

	Q $\left[\frac{l}{s}\right]$	q_s $\left[\frac{kg}{ms}\right]$	H [m]	U $\left[\frac{m}{s}\right]$	u_* $\left[\frac{m}{s}\right]$	C_f [-]	Re [10^3]	Re_* [-]	Fr [-]	H/R [-]	B/H [-]
H89	89	-	0.159	0.43	0.040	0.0086	68.4	80	0.34	0.094	8.2
M89	89	0.023	0.141	0.49	0.049	0.0100	68.4	97	0.41	0.083	9.2

[16] For the steady state in both experiments, nonintrusive measurements of three-dimensional velocity vector were made with high spatial and temporal resolution by means of an Acoustic Doppler Velocity Profiler (ADVP) developed at EPFL. The working principle of the ADVP, data treatment procedures and estimations of the accuracy in the flow variables have been reported by *Lemmin and Rolland* [1997], *Hurther and Lemmin* [1998], *Blanckaert and Graf* [2001], *Blanckaert and de Vriend* [2004], and *Blanckaert and Lemmin* [2006].

[17] The acquisition time was 180 s and measurements were made in the cross-sections at 15°, 30°, 60°, 90°, 120°, 150° and 180° in the bend. For the flat bed experiment, measurements in the straight reaches were made in the cross-sections 2.5 m and 0.5 m upstream of the bend and 0.5 m, 1.5 m, 2.5 m and 3.5 m downstream of the bend. For the equilibrium bed experiments, the measured cross-sections in the straight reaches were situated 2.2 m upstream of the bend as well as 0.5 m, 1.3 m, 2.2 m and 2.9 m downstream of the bend.

[18] In these cross-sections vertical profiles were measured on a grid that refines toward the banks including the verticals at, $n = \pm[0, 0.05, 0.1, 0.15, 0.2, 0.25, 0.3, 0.325, 0.35, 0.375, 0.4, 0.425, 0.45, 0.475, 0.5, 0.515, 0.53, 0.545, 0.56, 0.575, 0.59, 0.60, 0.61, 0.62]$ m. The reference system (s, n, z) is defined in Figure 1, which also summarizes the

hydraulic conditions in both experiments. Flow is subcritical ($Fr < 1$) and rough turbulent ($Re \gg 4,000$ and $Re_* > 70$).

3. Numerical Model and Simulation Setup

[19] The finite-differences RANS code [*Zeng et al.*, 2005a, 2008] used in the present work can predict flow, sediment transport and bathymetry in open-channel geometries with loose beds. The 3D incompressible RANS equations are expressed in generalized curvilinear coordinates with the so-called partial transformation, in which the spatial coordinates are transformed from Cartesian coordinates x_i into curvilinear coordinates ξ^i. The velocity components V_i in the momentum and in the other transport equations part of the model are left in Cartesian coordinates. The continuity and momentum equations are:

$$J \frac{\partial}{\partial \xi^j}\left(\frac{V^j}{J}\right) = 0 \tag{1}$$

$$\frac{\partial Q}{\partial t} + A_j \frac{\partial Q}{\partial \xi^j} - J \frac{\partial E_{vj}}{\partial \xi^j} + H_P = 0 \tag{2}$$

Once a length scale (H) and a velocity scale (U) are chosen, formally the Reynolds number $Re = UH/\nu$ replaces the molecular viscosity ν. In equation (2) $Q = (V_1, V_2, V_3)^T$ is the Cartesian velocity vector; J is the Jacobian of the geometric transformation, $V^i = V_j \xi^j_{x_i}$ are the contravariant velocity components, $E_{vj} = (E^1_{vj}, E^2_{vj}, E^3_{vj})$ are vectors representing the sum of the viscous and turbulent stresses, H_P is the (piezometric) pressure gradient vector, $A_j = \text{diag}(V^j, V^j, V^j)$ and $g^{ij} = \xi^i_{x_l} \xi^j_{x_l}$ is the contravariant metric tensor (summation over the l index).

[20] The turbulent stresses in E_{vj} are calculated with an eddy viscosity model. In the present code, the eddy viscosity is provided by the *k-ω Shear Stress Transport (SST)* model [*Menter*, 1994] or the Spalart-Almaras (SA) model [*Spalart*, 2000] in low-Reynolds number versions that have the capability to account for small-scale bed roughness effects through the boundary condition for the turbulence vorticity ω and, respectively, the modified eddy viscosity $\tilde{\nu}$ at the wall.

[21] As the standard form of the *k-ω SST* model was used, only the implementation of the boundary conditions (for a detailed discussion, see *Wilcox* [1993]) is discussed. At the walls the turbulent kinetic energy, k, is set equal to zero. For smooth surfaces ω is calculated as $\omega = 800\nu/(\Delta\zeta_1^2)$ where $\Delta\zeta_1$ is the distance to the wall of the first grid point situated off the wall. For rough surfaces, $\omega = 2500\nu/(k_s)^2$ for $k_s^+ < 25$ and $\omega = 100 u_\tau/k_s$ for $25 < k_s^+$, where k_s is the equivalent roughness height ($k_s^+ = u_\tau k_s/\nu$) and u_τ is the friction velocity.

[22] In the SA model [*Spalart*, 2000] only one transport equation is solved for the modified viscosity $\tilde{\nu}$. The transport equation for $\tilde{\nu}$ is:

$$\frac{\partial \tilde{\nu}}{\partial t} + V^j \frac{\partial \tilde{\nu}}{\partial \xi^j} = C_{b1}\tilde{S}\tilde{\nu} + \frac{1}{\sigma}\left[\nabla \cdot ((\nu + \tilde{\nu})\nabla\tilde{\nu}) + C_{b2}(\nabla\tilde{\nu})^2\right]$$
$$- C_{w1}f_w\left(\frac{\tilde{\nu}}{d}\right)^2 \tag{3}$$

where S is the magnitude of the vorticity and

$$\tilde{S} \equiv S + (\tilde{\nu}/\kappa^2 d^2) f_{v2}$$
$$f_{v2} = 1 - \tilde{\nu}/(1/Re + \tilde{\nu} f_{v1})$$
$$f_{v1} = \chi^3/(\chi^3 + C_{v1}^3)$$
$$\chi = \tilde{\nu}/\nu + 0.5\frac{k_s}{d}$$
$$f_w = g\left[\frac{1 + C_{w3}^6}{g^6 + C_{w3}^6}\right]^{\frac{1}{6}} \qquad (4)$$
$$g = r + C_{w2}(r^6 - r)$$
$$r \equiv \frac{\tilde{\nu}}{\tilde{S}\kappa^2 d^2}$$

The model constants in the above equations are $C_{b1} = 0.135$, $C_{b2} = 0.622$, $\sigma = 0.67$, $\kappa = 0.41$, $C_{v1} = 7.1$, $C_{w2} = 0.3$, $C_{w3} = 2.0$ and $C_{w1} = C_{b1}/\kappa^2 + (1 + C_{b2})/\sigma$. The eddy viscosity ν_t is obtained from

$$\nu_t = \tilde{\nu} f_{v1} \qquad (5)$$

To account for roughness effects, the modified distance to the wall is defined as $d = d_{min} + 0.03\, k_s$ where d_{min} is the distance to the nearest wall. Then, $\tilde{\nu}$ is set equal to zero at the smooth walls. For rough surfaces (e.g., the bed), the value of $\tilde{\nu}$ is estimated [Spalart, 2000] by solving $\partial \tilde{\nu}/\partial \zeta = \tilde{\nu}/d$, where ζ is the wall normal direction. This makes the modified viscosity and the eddy viscosity to be formally nonzero at the rough walls.

[23] If the equivalent bed roughness k_s cannot be estimated on the basis of experimental observations, k_s is calculated using a formula proposed by van Rijn [1984] in the case in which small bed forms that are not resolved by the grid deformations are present:

$$k_s = 3d_{90} + 1.1\Delta(1 - e^{-25\chi}) \qquad (6)$$

where the first term is the sand grain roughness contribution and the second term represents the bed form contribution. In equation (6), $\chi = \Delta/\lambda$ where Δ and λ are the estimated height and length of the sand waves, respectively. Following van Rijn [1984] and Wu et al. [2000] the length λ is assumed to be $\lambda = 7.3\, h$ and the parameter χ is estimated from:

$$\chi = \Delta/\lambda = 0.015(d_{50}/h)^{0.3}(1 - e^{-0.5T})(25 - T) \qquad (7)$$

in which h is local water depth, d_{50} and d_{90} are the median and 90% diameters of the bed material. The nondimensional excess shear stress, T, is defined as:

$$T = (u_\tau'^2 - u_{\tau cr}^2)/u_{\tau cr}^2 \qquad (8)$$

where $u_{\tau cr}$ is the critical bed-shear velocity for sediment motion given by Shields diagram and u_τ' is the effective bed friction velocity related to sand grain roughness. Following Wu et al. [2000], u_τ' is estimated as:

$$u_\tau' = U_s \sqrt{g}/C_{ch}' \qquad (9)$$

where $C_{ch}' = 18 \cdot \log(12R_b/k_s)$ is the sand grain Chezy coefficient, U_s is the depth-averaged streamwise velocity, R_b is the hydraulic radius and g is the gravitational acceleration.

[24] A fractional step method [Constantinescu and Squires, 2004] is used to solve the RANS equations. The continuity and momentum equations are discretized in delta form on a nonstaggered mesh. The momentum and transport equations are discretized using the second-order accurate upwind scheme for the convective terms. All the other discrete operators are calculated using the second-order central scheme. The momentum and the other transport equations for the turbulent quantities are advanced in pseudo-time implicitly using the alternate-direction-implicit (ADI) method. The deformations of the free surface are calculated from the kinematic and dynamic free surface conditions [nonhydrostatic model, Zeng et al., 2005a] or by using a rigid lid approximation and converting the pressure distribution into an equivalent free surface deformation (hydrostatic assumption). Both methods were used in the simulations of the flat bed experiment. The results (free surface deformation and velocity flow fields) were found to be very close. The rigid lid approximation was used in the simulations of the mobile bed experiment.

[25] In the present mobile bed simulation, the model of Engelund and Hansen [1967] was used to estimate the total sediment load. As no suspended sediment transport occurred in the experiment simulated here, the total sediment load is equal to the bed load and no empirical formula is needed to split the total load into its two components. It is important to mention that for cases in which suspended sediment transport is significant [e.g., Zeng et al., 2008], we are using the nonequilibrium bed load transport model of van Rijn (see [Wu et al., 2000] for a complete description) coupled with a transport equation for the concentration of the suspended sediment. Both Zeng et al. [2005b] and Wu et al. [2000] have shown that ignoring the suspended sediment transport does not change significantly the equilibrium bathymetry predictions if the bed load accounts for more than 75% of the total sediment load. Moreover, for cases in which the suspended load is negligible, the model of Engelund and Hansen [1967] was proved to give comparable or slightly better predictions than the van Rijn model [e.g., see Zeng, 2006 who predicted using both models the equilibrium flow and sediment transport in the 140° curved bend with loose bed studied experimentally by Struiksma, 1983]. This is despite the fact that the model of Engelund and Hansen [1967] predicts a nonzero sediment transport rate if the Shields parameter is below critical. By comparison, van Rijn's model correctly handles the case when the Shields parameter is below critical.

[26] Engelund and Hansen [1967] estimate the magnitude of the total sediment load, Q_b, as:

$$Q_b = 0.05\sqrt{R_0 g d_{50}^3}\frac{C_{ch}'^2}{g}(\theta)^{2.5} \qquad (10)$$

where $\theta = \tau_b/(R_0 \rho g d_{50})$, $R_0 = (\rho_s/\rho) - 1$, τ_b is the bed shear stress and ρ_s is the sediment density.

[27] The direction of the bed load transport accounts for down-slope gravitational force effects by means of the model of Sekine and Parker [1992]. This model provides the ratio between the streamwise ($Q_{b\xi}$) and transverse ($Q_{b\eta}$) components of the bed load vector as a function of the local orientation of the bed shear stress vector, the streamwise

$(\partial z_b/\partial l_\xi)$ and transverse $(\partial z_b/\partial l_\eta)$ bed slopes, and the critical Shields stress.

$$Q_{b\eta}/Q_{b\xi} = \left(\sin\theta_b - \beta\frac{\partial z_b}{\partial l_\eta}\right)\Big/\left(\cos\theta_b - \beta\frac{\partial z_b}{\partial l_\xi}\right) \quad (11)$$

In equation (11), θ_b is the angle between the bed shear stress vector and the streamwise direction, $\beta = \beta^*(\tau_c^*/\tau_L^*)^m$, τ_L^* is the longitudinal Shield stress $\tau_L^* = \tau_b\cos\theta_b/\rho R_0 g d_{50}$, $\tau_c^* = \rho u_{\tau cr}^2/\rho R_0 g d_{50}$, m is a coefficient which is taken equal to unity in the present implementation of the model, and $\beta^* = \alpha_G/\tau_c^*$. Finally, α_G is a coefficient typically in the range of 0.45 to 0.7. Consistent with the other validation test cases, in all the simulations with the SA model we used $\alpha_G = 0.6$, while in all the k-ω SST simulations the value of α_G was 0.45. Despite possible errors in the estimation of the flow velocities in the near bed region, accounting for gravitational bed slope effects was found to be essential to obtain good predictions of the bathymetry at equilibrium conditions. This is consistent with the findings in the studies of *Ruther and Olsen* [2005] and *Zeng et al.* [2008]. Using equations (10) and (11), one can estimate $Q_{b\xi}$ and $Q_{b\eta}$.

[28] The changes in the bed elevation, z_b, are calculated from the mass balance equation for the sediment in the bed load layer in which the storage term is neglected and the net flux of sediment at the top of the bed layer is assumed to be zero (suspended sediment transport is neglected in the present simulations):

$$(1 - p')\frac{\partial z_b}{\partial t} = -\nabla\vec{Q}_b = -J_b\left(\frac{\partial}{\partial\xi}\left(\frac{Q_{b\xi}}{J_b}\right) + \frac{\partial}{\partial\eta}\left(\frac{Q_{b\eta}}{J_b}\right)\right) \quad (12)$$

where p' (=0.7) is the porosity of the bed material, J_b is the Jacobian of the geometric transformation corresponding to the 2D bed grid, z_b is the bed level above a datum. Once z_b and the free surface level are calculated, the grid points between the bed level and the free surface are redistributed vertically based on the positions of the water surface and bed level elevations using a hyperbolic stretching function. In the present study in which one is interested in the final equilibrium state of the flow and the bathymetry, only the steady state algorithms are used (the equations that are solved do not include the terms accounting for the grid deformation in a time-accurate way).

[29] Validation of the code for open-channel geometries with fixed and loose beds is described by *Zeng et al.* [2005a, 2005b, 2008] and *Zeng* [2006]. They include prediction of the flow, water surface deformation, sediment transport and equilibrium bathymetry in the moderately curved open channels studied experimentally by *Yen* [1967], *Struiksma* [1983], *Odgaard and Bergs* [1988], and *Olesen* [1985] for which good agreement with experimental data was obtained.

[30] The numerical predictions are obtained without assuming that the law of the wall is valid. This is possible because the present model uses RANS models in low-Reynolds number versions that can account for the effects of (sand grain and small bed forms) bed roughness and the mesh in the wall normal direction is fine enough such that the use of wall functions can be avoided.

[31] The flow in the flat bed experiment was simulated on a computational mesh with 380,000 grid points (109 × 101 × 35 mesh points in the streamwise, spanwise and vertical

directions, respectively). As the k-ω SST and the SA results were similar, we report in this paper only the SA results. The inflow section was situated at 2.5 m upstream of the bend entrance (section M2.5). The water depth and mean velocity measurements available at this section were used to specify the inflow boundary conditions. Inflow boundary conditions for the turbulence quantities for which transport equations (e.g., $\tilde{\nu}$ for the SA model) are solved were specified on the basis of a fully developed turbulent flow solution obtained in a straight channel of identical section in which periodic boundary conditions were used in the streamwise direction. The first array of grid points off the side-walls and channel bed were situated at $\Delta\zeta/H \sim 0.00037$ ($\Delta\zeta^+ \sim 1.0$ wall unit). The value of the equivalent roughness at the bed was estimated as $k_s = 0.0022$ m ($\sim d_{90}$). All velocity components were set equal to zero on the wall surfaces (no slip) including the channel bed. Zero gradient boundary conditions were used at the outlet section for all the variables.

[32] The flow, sediment transport and bathymetry at equilibrium conditions in the mobile bed experiment were simulated on a computational mesh with close to 450,000 grid points (127 × 101 × 35). Predicted equilibrium bathymetry profiles are reported for both k-ω SST and the SA turbulence closure models because accurate prediction of this quantity is essential for the validation of the loose bed RANS model. Since bathymetry predictions by both models were similar, the other flow quantities are reported only for the SA simulation. The inflow section in the mobile bed simulation was situated at the flume entrance (9 m upstream of the bend entrance), where distributions of the mean velocity and turbulence variables corresponding to fully developed turbulent flow were obtained from a preliminary straight channel simulation and the measured bed load inflow rate of $q_s = 0.023$ kgm^{-1} s^{-1} was imposed. The first array of grid points off the lateral walls and channel bed was situated at $\Delta\zeta/H \sim 0.00037$ during the iterative process in which the bed elevation evolved toward equilibrium. The value of the equivalent bed roughness was estimated as $k_s \sim 0.037$ m (sand-grain roughness plus contribution from small unresolved bed forms) from equation (6) using mean values for h and u_τ in the straight inflow reach. This value is comparable with the measured height (0.03–0.05 m) of the small-scale traveling dunes observed over the whole channel bend length in the experiment. The mobile bed simulations started from an initial condition with flat bed and with a layer of 35 cm of sand. The simulations were run until the flow and bathymetry reached steady state corresponding to equilibrium conditions.

[33] As the turbulent kinetic energy k is not directly available from the SA model simulations, it was estimated in an indirect way. The converged velocity field and bathymetry (deformable bed simulation only) from the SA simulation were frozen, and the transport equations corresponding to the k and ω equations in the k-ω SST model were solved until a converged solution for the k and ω fields was reached.

[34] Before discussing the simulation results, the main modeling assumptions of the model are discussed.

[35] The coupling between the flow and the sediment model occurs mainly through the changes in bed elevation. As the bathymetry changes, the distribution of the velocity field in the channel is affected. This, in turn, modifies the

distribution of the bed shear stress (magnitude and direction), the local value of the depth averaged streamwise velocity in equation (9), the local value of Q_b in equation (10) and the local value of the splitting ratio between the streamwise and transversal components of Q_b in equation (11). Finally, the distributions of $Q_{b\xi}$ and $Q_{b\eta}$ determine the new position of the bed elevation (equation (12)). With respect to this dominant flow-sediment interaction, effects such as the influence of the sediment on the turbulent flow structure or the additional drag needed to carry the particles in suspension are assumed to be negligible. All previous 3D numerical studies of flow in bends with movable bed [e.g., *Wu et al.*, 2000; *Ruther and Olsen*, 2006; *Khosronejad et al.*, 2007] employ this assumption. In these models the flow fields are obtained by solving the Navier-Stokes equations similar to the case when sediment is absent. The sediment transport is divided into the bed load and suspended load components. Finally, the bed elevation changes are calculated from a mass balance equation for the sediment. The use in our solver of more complex turbulence models (e.g., two-equation RANS models in versions that do not need the use of wall functions) and relatively fine meshes required by these models results in a more accurate prediction of the flow field for a given shape of the bathymetry. This translates into more accurate predictions of the bed shear stress and depth-averaged streamwise velocity distributions used by the sediment transport model. In particular, the use of a more complex turbulence model allows estimating more accurately the cross-stream flow and the bed shear stress deviation from the mean flow direction due to cross-stream motions (in 2D depth-averaged models empirical models that characterize the intensity of the cross-stream flows have to be used which is a major deficiency of these models).

[36] The most problematic part of the approach described above is the highly empirical nature of the equations used to model the bed-load or the total-load sediment rate and the fact that these equations and their parameters were calibrated based on data obtained for flow in straight channels or mildly curved river bends. When these formulae are used in numerical models one has to be aware of the range of conditions (e.g., particular range of sediment sizes and flow conditions) and specific assumptions used to deduce them. If the suspended sediment load is nonnegligible and a total sediment-load formula is used, the splitting between the bed load and the suspended sediment load is generally done in an empirical manner. In the application reported in the present paper the suspended sediment load was negligible, so this was not an issue. Accounting for nonequilibrium effects and using an appropriate model to specify the nonequilibrium adaptation length are very important if the bathymetry evolution is simulated in a time-accurate way and flow conditions are unsteady (e.g., simulation of flood events). However, for the present simulations in which the goal is only to predict the steady-state equilibrium flow, sediment transport and bathymetry, the use a sediment transport model that can account for nonequilibrium effects is not necessary. Another critical factor is the effect of bed slope which influences both the sediment transport rate and its direction. Though several models have been proposed, they are all semi empirical. The model used in the present work [*Sekine and Parker*, 1992] contains one such empirical parameter, α_G. For a given turbulence model, the value of

α_G was calibrated [*Zeng*, 2006] based on simulations of the flow in an 180° bend studied experimentally by *Odgaard and Bergs* [1988]. All the other applications [e.g., *Zeng*, 2006] of the present model for loose-bed simulations used the same value for this parameter. Finally, the specification of the bed roughness contribution from small unresolved bed forms or due to the presence of small-scale traveling bed forms can be an additional source of errors. In the present simulations the uncertainty of accounting for such effects was reduced by the fact that an estimation of the height of the small-scale traveling dunes was available from experiment. The present model is also limited to applications in which the size of the sediment can be considered close to uniform.

4. Sharp Open-Channel Bend With Flat Bed

[37] The objectives of this section are mainly to provide experimental data that highlights flow processes in sharp open-channel bends with flat bed and to validate the hydrodynamics module of the numerical model by means of comparing measured and predicted distributions of the most relevant flow parameters and processes.

[38] Figure 2 shows the measured and predicted distributions of the normalized depth-averaged streamwise velocity, U_s/U, around the flume, which are similar to the distributions of the normalized streamwise unit discharge $U_s h/(UH)$ for the flat bed configuration (h is the local flow depth). Four mechanisms identified by *Johannesson and Parker* [1989] contribute to the measured curvature induced redistribution over the width of the streamwise velocity (Figure 2):

[39] 1. The shorter distance in the inner bend than in the outer bend would lead to a potential vortex distribution, with U_s decreasing from the inner toward the outer bank [*Rozovskii*, 1957; *Henderson*, 1966]. Such a distribution is measured just downstream of the bend entrance, where it is created by the pronounced flow acceleration/deceleration in the inner/outer half of the cross-section. This flow acceleration/deceleration is induced by streamwise pressure gradients related to the sudden transverse tilting of the water surface in the bend.

[40] 2. At the bend exit, the sudden disappearance of the transverse tilting of the water surface leads to pronounced flow accelerations/decelerations in the outer/inner half of the cross-section.

[41] 3. Higher flow depths attract higher velocities, as indicated by Chézy's law for example ($U_s \sim h^{1/2}$). This mechanism is dominant over a mobile bed but negligible over a flat bed.

[42] 4. Curvature induced cross-stream circulation is a characteristic feature of curved open-channel flow. Advective transport of streamwise momentum by the cross-stream circulation is known to lead to an outward shift of the core of high velocities in open-channel bends. This mechanism is responsible for the measured gradual outward shift of the core of high streamwise velocities around the bend. Since the curvature induced cross-stream circulation persists some distance downstream of the bend, the core of high streamwise velocities continues shifting in the outward direction for some distance in the straight outflow reach. Some differences are observed between the measured and predicted gradual outward shift of the core of high velocities.
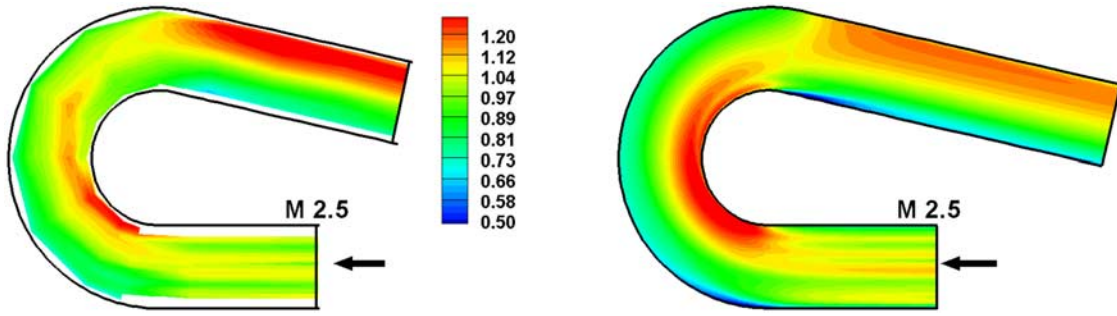
Figure 2. Distribution of the normalized depth-averaged streamwise velocity, U_s/U in the bend with flat bed. (left) Based on measurements. (right) Predicted.

[43] The outward transport of streamwise momentum by the cross-stream circulation is a subtle process that depends on the magnitude of the cross-stream circulation and on the nonlinear interaction between the vertical profiles of the streamwise velocities, v_s, and transverse velocities, v_n [*de Vriend*, 1981a, 1981b; *Blanckaert and de Vriend*, 2003; *Blanckaert and Graf*, 2004]. Measured and predicted distributions of these flow characteristics will now be analyzed and compared.

[44] Figure 3 shows the measured and predicted evolutions around the flume of the normalized depth-averaged cross-stream circulation strength, parameterized by means of the function ψ, defined as:

$$\psi = \frac{1}{2}(\psi_n + \psi_z) \qquad (13)$$

$$\psi_n = -(1 + n/R)\int_{z_b}^{z} v_n^* dz \qquad (14)$$

$$\psi_z = \int_{-B/2}^{n} (1 + n/R)v_z dn + A \qquad (15)$$

where v_n^* represents the circulatory part of the transverse velocity, obtained by subtracting the depth-averaged part U_n from the total transverse velocity v_n, v_z is the vertical velocity component, and R is the curvature radius of the bend. The integration constant, A, in equation (15) is chosen such that the cross-sectional-averaged values of ψ_n and ψ_z

are equal. In fully-developed curved flow ($\partial/\partial s = 0$, infinite bend), $\psi_n = \psi_z$ and ψ represents the classical definition of the streamfunction [*Batchelor*, 1967]. This is why the function ψ will be called the pseudo-streamfunction hereafter. The pseudo-streamfunction has already been applied to visualize and quantify patterns of cross-stream circulation in other experiments [e.g., *Blanckaert et al.*, 2008].

[45] Upon entering the bend, the cross-stream circulation assumes nonzero values and increases about linearly. Although the driving curvature is constant around the bend, the cross-stream circulation reaches a maximum value in the cross-section at 90° and subsequently decreases significantly, to about half its maximum value at the bend exit. In the straight outflow reach, the cross-stream circulation further decays and disappears. The cell of large cross-stream circulation values occupies the major part of the cross-section. From the bend entry onto the cross-section at 90°, it is about symmetrically positioned in the cross-section. Further downstream, the center of the circulation cell shifts outward, as if it follows the core of high streamwise velocity.

[46] Near the outer bank, a weaker counter-rotating cell of cross-stream circulation is discernable, which is called outer-bank cell. Such an outer-bank cell has been observed in the field by *Bathurst et al.* [1979], *Dietrich and Smith* [1983], and *de Vriend and Geldof* [1983]. The outer-bank cell is relevant with respect to the shear stress at the outer bank. The outer-bank cell is not captured by the simulations. This is in agreement with *Blanckaert and de Vriend* [2004] who have analyzed the mechanisms underlying the formation of the outer-bank cell and postulated that higher-order turbulence models that resolve turbulence anisotropy and
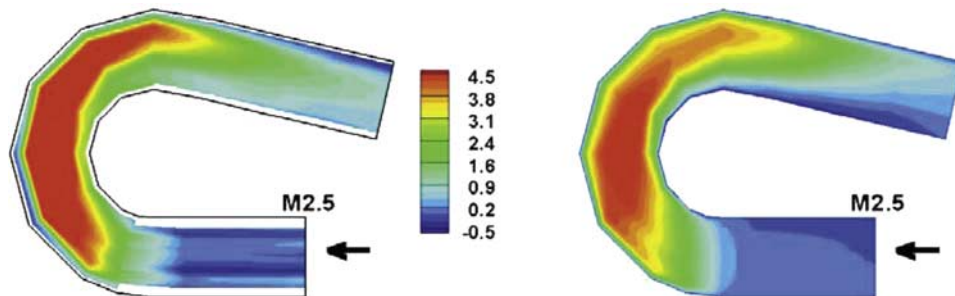

Figure 3. Distribution of the normalized depth-averaged cross-stream circulation strength, $100\langle\psi\rangle/(UH)$ in the bend with flat bed. (left) Based on measurements. (right) Predicted.
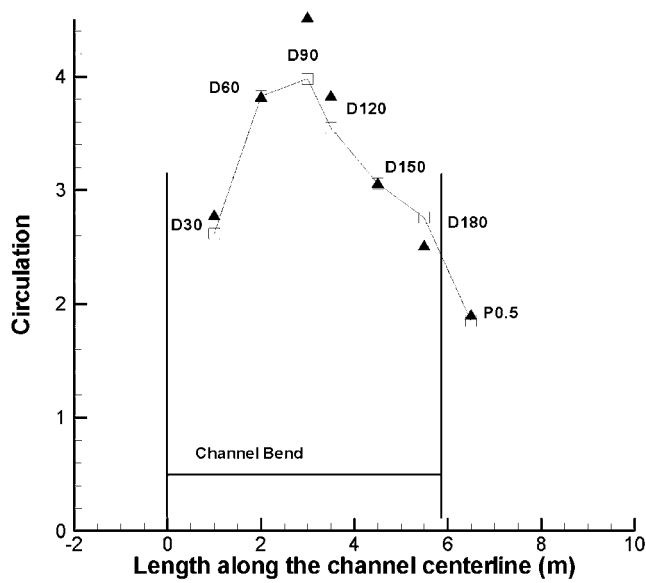
Figure 4. Variation along the bend of the circulation associated with the patch of positive streamwise vorticity corresponding to the main cell of cross-stream circulation. The filled triangles correspond to the experiment. The squares correspond to the simulation.

the kinetic energy transfer between mean flow and turbulence are required to capture the outer-bank cell.

[47] The model predicts the strong increase of the cross-stream circulation cell in the first part of the bend, the location where it reaches maximum strength as well as its subsequent decay. It also captures the central position over the width in the first part of the bend and the subsequent outward shift of the core of maximum values. However, the model seems to underestimate systematically the values in the center of the circulation cell from the bend entry onto the cross-section at 180°. This underestimation is only partially compensated by the overestimation of the width of the cross-stream circulation cell.

[48] The pseudo-streamfunction is equivalent to the streamwise vorticity, $\omega_s = \partial v_z/\partial n - \partial v_n/\partial z$ [see *de Vriend*, 1981a, 1981b]. The pseudo-streamfunction has the advantages of being a scalar quantity, in contrast to the cross-stream circulation vector (v_n^*, v_z), and of being computable with less uncertainty from experimental data characterized by scatter: integration of the measured velocity field reduces scatter, whereas taking the derivatives of the measured velocity field amplifies it. However, the streamwise vorticity defines more rigorously the cross-stream circulation and has a clearer physical meaning.

[49] Figure 4 shows the variation along the channel bend of the circulation (integral of the streamwise vorticity) associated with the patch of positive vorticity (excluding the contribution of the outer-bank cell), which directly characterizes the overall intensity of the cross-stream motions. The circulation peaks in the cross-section at 90° in both experiment and simulation. The value of the maximum circulation is underpredicted by about 10%. The agreement is better at the other sections inside the curved reach, both upstream and downstream of the cross-section at 90°.

[50] Integrating over the zone covered by the cross-stream circulation improves the agreement between measurements and predictions (see Figures 3 and 4), which means that the numerical model successfully captures the strength of the cross-stream motions in an average or integral sense. There seems to be a systematic tendency to underpredict the maximum values of the cross-stream circulation, which is consistent with the underestimation of the outward shift of the core of high streamwise velocities in Figure 2.

[51] *Blanckaert and de Vriend* [2003] and *Blanckaert and Graf* [2004] have attributed the evolution of the cross-stream circulation and streamwise vorticity to the interaction between the vertical profiles of the streamwise (v_s) and transverse (v_n) velocities. Advective momentum transport by the cross-stream circulation flattens the streamwise velocity profiles, by increasing/decreasing velocities in the lower/upper part of the water column. The flattening of the v_s-profile reduces the driving force for the cross-stream circulation.

[52] The importance of the vertical profiles of v_s and v_n merits the comparison between measurements and predictions in Figures 5 and 7, respectively. In these and subsequent figures, the position of the vertical profile in the transverse (n) direction in a particular section is given in nondimensional form as η/H, with $-B/2 < \eta < B/2$.

[53] The vertical profiles of the streamwise velocity v_s are about logarithmic in the straight inflow reach, and subsequently flatten progressively around the bend. This flattening is particularly pronounced in the inner half of the cross-section, where the v_s-profiles downstream of the cross-section at 90° are nonmonotonic with maximum velocities in the lower part of the water column. In the straight outflow reach, the flattening decreases and the v_s-profiles evolve toward a logarithmic profile.

[54] Overall, Figure 5 shows local differences between measured and predicted profiles of v_s that are typically less than 10%. Some deviation occurs near the water surface close to the outer bank, where predicted profiles do not show the measured decrease of v_s toward the water surface (e.g., see cross-section at 180°). The flattening around the bend of the v_s-profiles is visualized in Figure 6, which shows the streamwise evolution of the normalized width-averaged profiles of the predicted streamwise velocity.

[55] Figure 7 compares measured and predicted vertical profiles of the normalized transverse velocity, v_n/U. Although the predictions seem to underestimate somewhat the transverse velocity and, locally, deviations between measured and predicted transverse velocities attain 30%, the simulation captures the main features of the curvature induced cross-stream circulation cell, which covers the major part of the cross-section and is characterized by outward/inward transverse velocities in the upper/lower part of the water column.

[56] The reversal of the measured vertical gradient $\partial v_n/\partial z$ in the corner formed by the outer bank and the water surface reveals the existence of the outer-bank cell of cross-stream circulation, which is not predicted by the numerical model (see contours of ψ in Figure 8). This is related to and consistent with the inability of the model to capture the decrease of streamwise velocities toward the water surface in this zone (Figure 5).
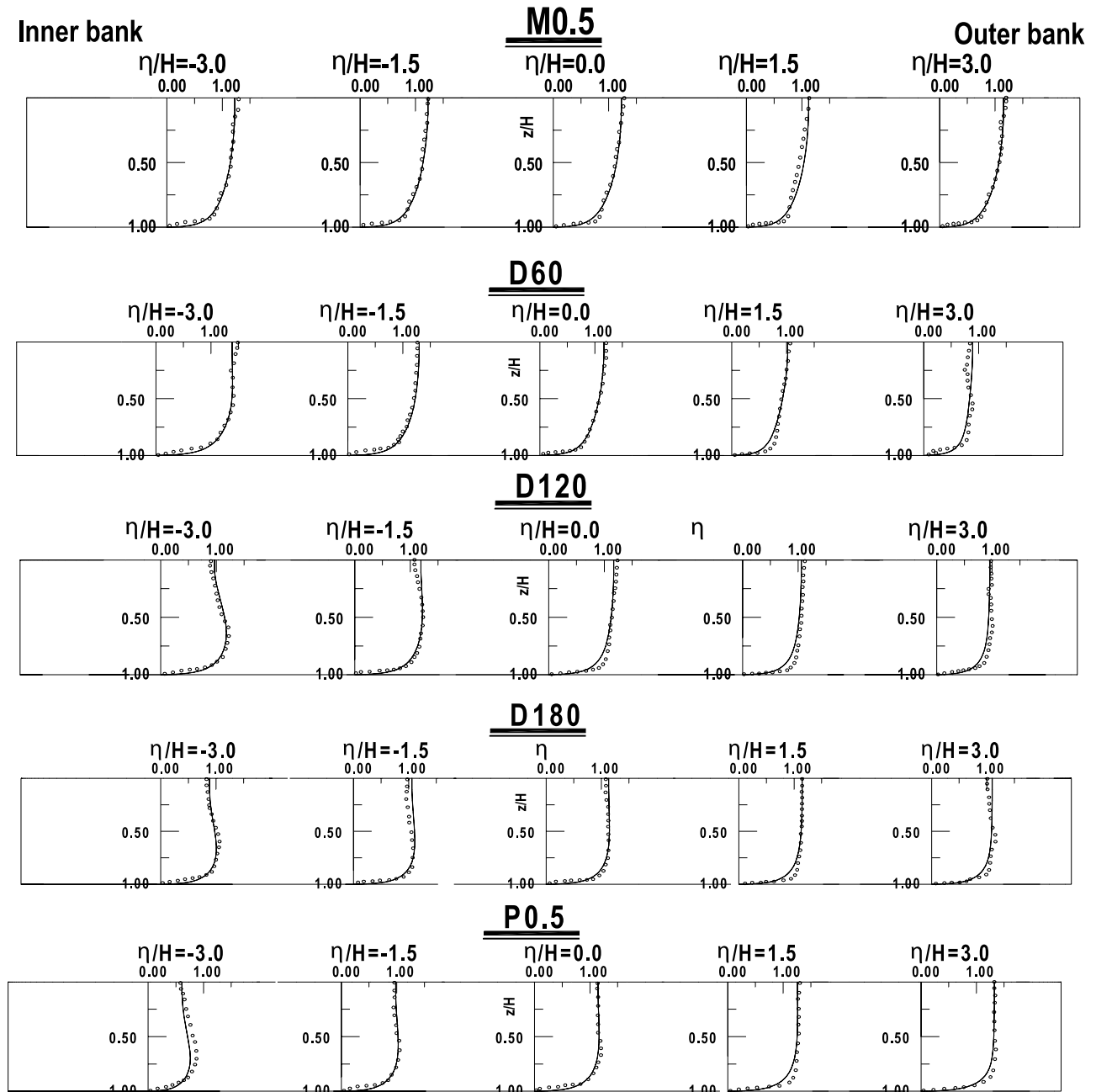
Figure 5. Comparison between measured (symbols) and predicted (solid lines) vertical profiles of the normalized streamwise velocity, v_s/U, in several cross-sections along the bend with flat bed.

[57] Figure 8 focuses on the measured and predicted patterns of the streamwise velocity, the cross-stream circulation, and the streamwise vorticity in the cross-section at 90°, where the strength of the cross-stream circulation is the highest (see Figures 3 and 4).

[58] The dominant character of advective momentum transport by the cross-stream circulation is clearly visible in the inclination of the v_s-isolines: momentum is advected in the outward/inward direction in the upper/lower part of the water column. This advective momentum transport leads to the deformation of the v_s-profiles described above (see Figures 5 and 6). The stretching of the core of high velocities leads to the formation of a core of low velocities in the corner formed by the inner bank and the water surface. However,

the flow does not separate from the inner bank. The pattern of cross-stream circulation in the cross-section at 90° is visualized by means of the pseudo-streamfunction ψ and the streamwise vorticity ω_s. The measured patterns illustrate the center-region cell of cross-stream circulation, which occupies the major part of the cross-section and is about symmetrically positioned. Besides, it visualizes very well the outer bank cell.

[59] Both experiment and simulation predict the formation of an elongated patch of positive streamwise vorticity situated in the lower part of the section. The vorticity levels inside the patch of positive vorticity are larger in the region close to the inner bank.
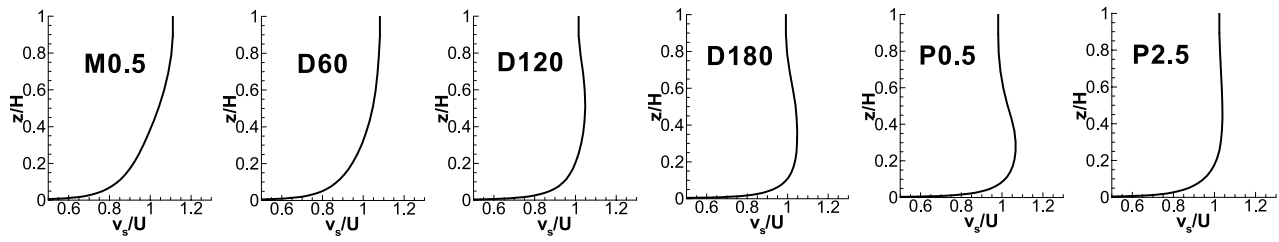
Figure 6. Predicted width-averaged profiles of the normalized streamwise velocity, v_s/U, in several cross-sections along the bend with flat bed.
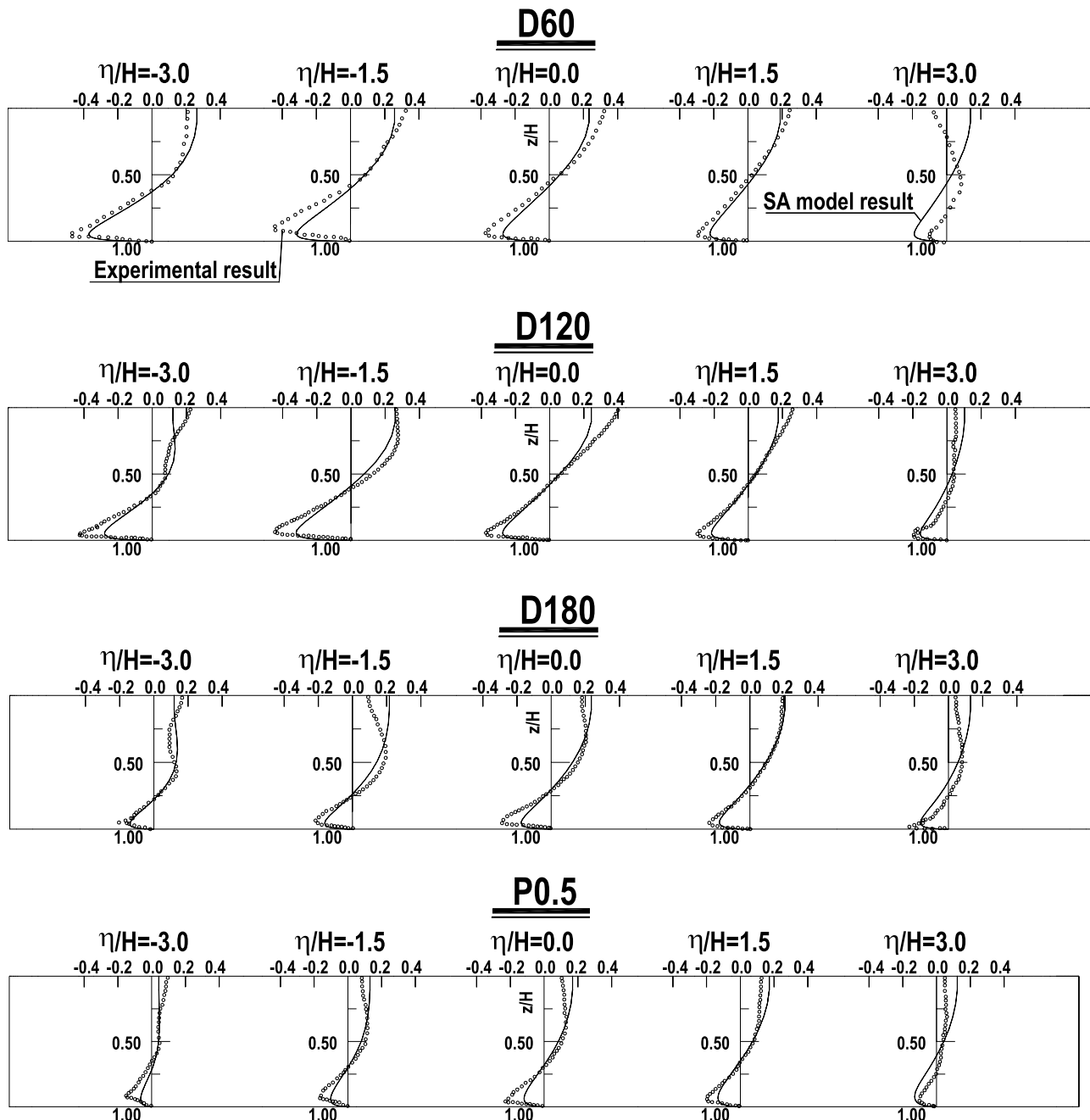

Figure 7. Comparison between measured (symbols) and predicted (solid lines) vertical profiles of the normalized transverse velocity, v_n/U, in several cross-sections along the bend with flat bed.
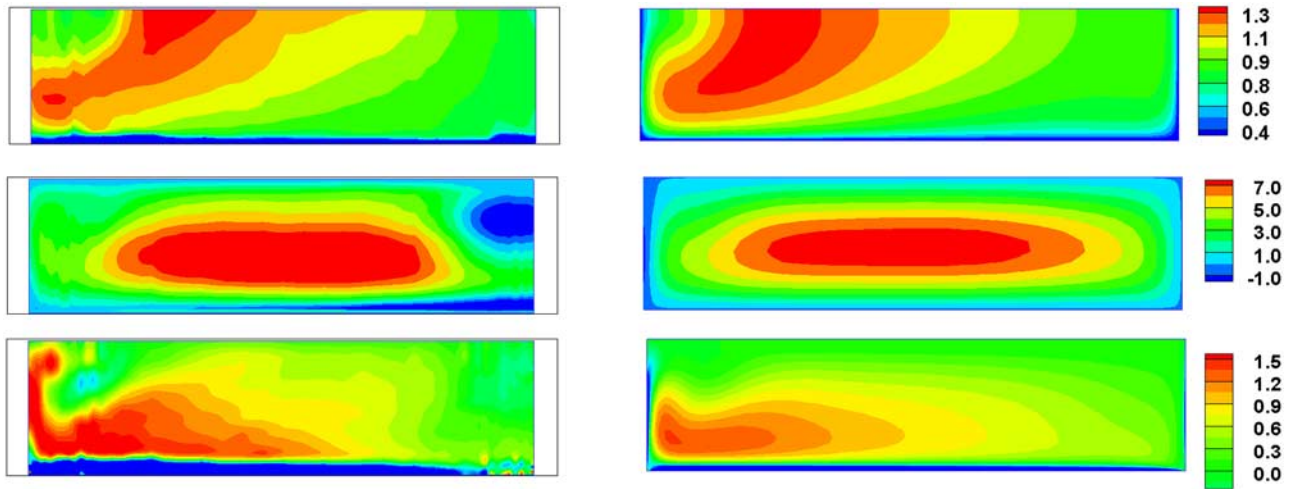
Figure 8. Comparison between (left) measured and (right) predicted patterns of the (top) normalized streamwise velocity v_s/U, (middle) normalized cross-stream circulation, $100\psi/(UH)$, and (bottom) streamwise vorticity $\omega_s(H/U)$, in the cross-section at 90° in the bend with flat bed.

[60] The distributions of the streamwise velocity and streamwise vorticity in the cross-section at 180° are shown in Figure 9. Compared to the cross-section at 90°, the core of maximum streamwise velocity has shifted toward the outer wall. The main patch of positive vorticity is more elongated, extends further toward the outer wall, and is situated closer to the bed. Compared to the experiment, the predicted streamwise vorticity gradients appear to be somewhat milder inside the patch of positive vorticity.

[61] Turbulence is relevant in river systems, with respect to entrainment and transport of sediment, mixing and spreading of pollutants and nutrients, ecological parameters and energy losses. Figure 10 shows the distribution around the flume of the normalized depth-averaged turbulent kinetic energy, $\langle k \rangle/(1/2u_*^2)$, which is a good indicator of turbulence activity.

[62] Turbulence activity increases strongly upon entering the bend and $\langle k \rangle/(1/2u_*^2)$ reaches maximum measured values in the bend reach from 90° to 150° that are about three times higher than in the straight approach flow. Downstream of the cross-section at 150°, $\langle k \rangle/(1/2u_*^2)$ decreases and is reduced to about half its maximum value at the bend exit.

Turbulence activity in the straight outflow reach remains slightly higher than in the straight inflow reach. The numerical model slightly underestimates maximum values of $\langle k \rangle/(1/2u_*^2)$ in the bend and in the straight outflow. The predicted maximum values of $\langle k \rangle/(1/2u_*^2)$ occur further downstream than the measured ones.

[63] Figure 11 shows satisfactory agreement between the measured and predicted patterns of normalized turbulent kinetic energy, $k/(1/2u_*^2)$ in the cross-section at 90° in the bend. A core of high turbulent kinetic energy (*tke*) exists, that seems to correspond to the core of the center region cell of cross-stream circulation. Profiles of *tke* do not monotonically decrease from the top of the bed inner layer toward the water surface as in straight uniform flows, but have maximum values around mid depth. *Blanckaert and de Vriend* [2005a, 2005b] have analyzed mechanisms underlying patterns and profiles of *tke* in sharply curved open-channel flow.

[64] Figures 3, 8, 10, and 11 indicate a relation between the turbulence activity and the strength of the cross-stream circulation. It can be postulated that strain rates $\partial v_n/\partial z + \partial v_z/\partial n$ induced by the cross-stream circulation contribute
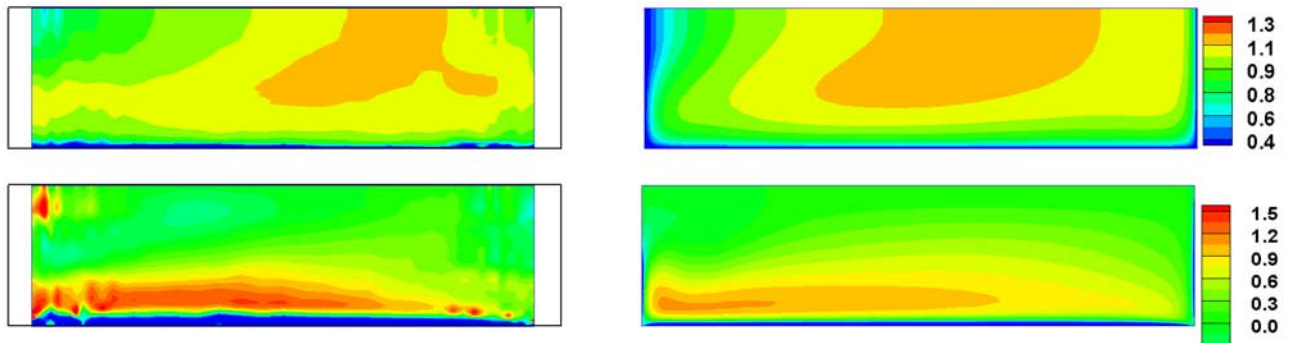

Figure 9. Comparison between (left) measured and (right) predicted patterns of the (top) normalized streamwise velocity v_s/U and (bottom) streamwise vorticity $\omega_s(H/U)$, in the cross-section at 180° in the bend with flat bed.
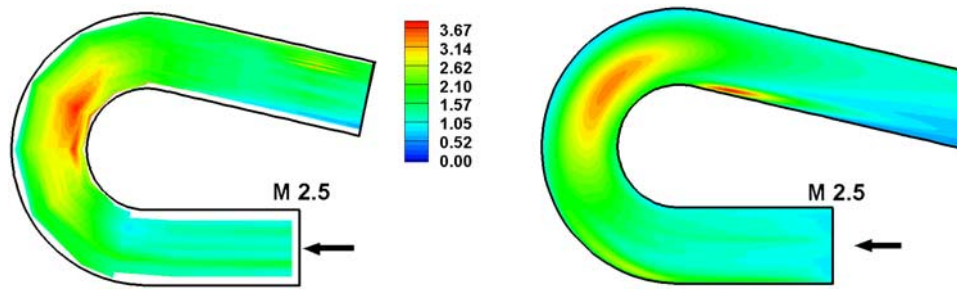
Figure 10. Distribution of the normalized depth-averaged turbulent kinetic energy, $\langle k \rangle / (1/2 u_*^2)$ in the bend with flat bed. (left) Based on measurements. (right) Predicted.

significantly to the production of *tke* through the production term $(\partial v_n / \partial z + \partial v_z / \partial n) . \overline{v_n' v_z'}$.

5. Sharp Open-Channel Bend With Equilibrium Bed

[65] The objective of this section is mainly to validate the hydrodynamics, sediment transport and bathymetry modules of the numerical model by means of comparing measured and predicted distributions of the bathymetry and the most relevant flow parameters and processes for the steady equilibrium configuration.

[66] To isolate the influences of the bathymetry and the flow field in the interpretation of discrepancies between measurements and predictions, the 3D morphodynamic model was applied in two phases: (1) prediction of the flow field over the prescribed measured equilibrium bathymetry and (2) prediction of the flow field and the equilibrium bathymetry.

[67] Figure 12 compares the measured and predicted equilibrium bathymetries in various cross-sections around the flume. Predictions are shown for simulations in which the *SA* and the *k-ω SST* turbulence closure models were employed.

[68] The bathymetry in open-channel bends is characterized by a transverse bed slope, which is determined by the interplay between the upslope transverse component of the bed shear stress induced by the cross-stream circulation and the down-slope gravitational pull on the sediment particles. The description of the measured bathymetry and the model validation will focus on the evolution of the maximum scour depth around the bend, which is the major parameter with respect to river engineering.

[69] Scour in the outer half of the cross-section develops upon entering the bend and reaches a maximum depth of about $2H$ (flow depth of about $3H$) in the cross-section at $60°$, before reducing to a value of about $1.2H$ (flow depth of about $2.2H$) in the cross-sections at $120°$ and $150°$. Scour increases again upon approaching the bend exit and reaches a depth of about $1.6H$ (flow depth of about $2.6H$) in the

cross-section at $180°$. Scour decays in the straight outflow reach and the bed is about flat in the outer part of section P2.9 situated 2.9 m downstream of the curved reach exit.

[70] Scour in the outer half of the cross-section is balanced by sediment deposition in the inner half of the cross-section. The flow depth at the centerline remains about constant at about $1H$, as postulated by *Odgaard* [1986, 1989]. The cross-sectional flow area, however, increases significantly in the curved reach.

[71] This observed behavior is in agreement with theoretical model concepts [*de Vriend and Struiksma*, 1984; *Struiksma et al.*, 1985; *Odgaard*, 1986] that predict an evolution toward the equilibrium scour depth in a damped oscillated way, including an overshoot of the equilibrium scour depth in the first part of the bend. The increasing scour depth near the bend exit (section D193) may partially be attributed to the flow accelerations in the outer half of the cross-section induced by the sudden disappearance of streamline curvature and the related superelevation of the water surface.

[72] The transverse bed profiles in the regions where scour occurs are well predicted over most of the flow width, and deviations are mainly concentrated in the region near the outer bank where the maximum scour depth occurs. The model predicts well the equilibrium flow depth of about $2.2H$, but underestimates the oscillation of the flow depth around the flume. In particular, the maximum flow depth of about $3H$ is underestimated by about 20% in the *SA* model simulation and by about 30% in the *k-ω SST* model simulation.

[73] In a similar way, sediment deposition on the point bar in the inner half of the cross-section is underestimated in some sections and overestimated in others. This is less important however, since flow over the shallow inner part of the cross-section hardly contributes to the discharge (see later). These shallow flow regions are difficult to simulate accurately using a model that accounts for local changes in bathymetry by redistributing points in the vertical direction. As the maximum scour depth is consistently underpre-
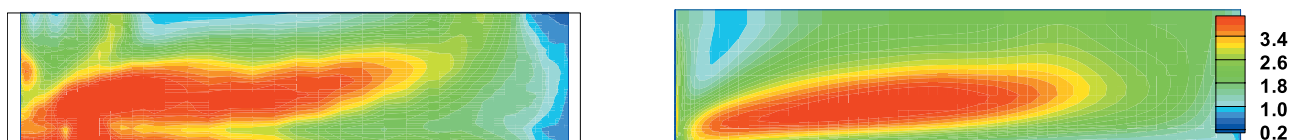

Figure 11. Comparison between (left) measured and (right) predicted patterns of the normalized turbulent kinetic energy $k/(1/2 u_*^2)$ in the cross-section at $90°$ in the bend with flat bed.
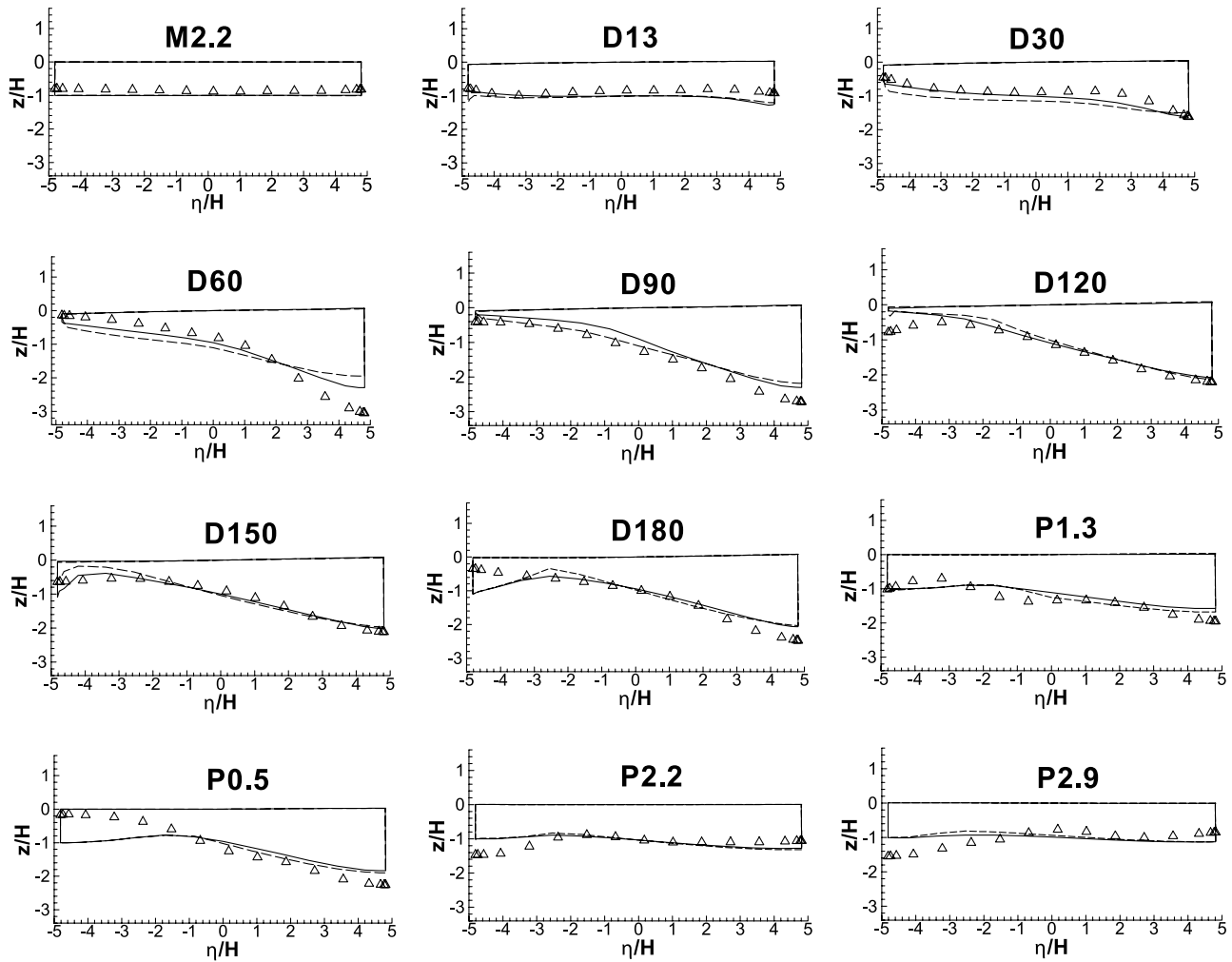
Figure 12. Equilibrium bathymetry. Measured (symbols) and predicted by means of the *SA* model (solid lines) and the *k-ω SST* model (dashed lines).

dicted, it is expected that by decreasing the value of the constant in the model of *Sekine and Parker* [1992] one can further improve the overall agreement. However, in the present simulations the same value of the model coefficient was used as in the previous test cases conducted in moderately curved bends [*Zeng et al.*, 2005a, 2008].

[74] Since differences between predictions with the *SA* and *k-ω SST* turbulence closure models are not significant, only predictions with the *SA* model will be shown hereafter for the analysis of flow parameters.

[75] Whereas advective momentum transport by the cross-stream circulation was the dominant mechanism with respect to the outward redistribution of depth-averaged streamwise unit discharge, $q_s = U_s h$, in the flat bed configuration, this flow parameter is strongly conditioned by the bathymetry in the equilibrium bed configuration (see Figure 13).

[76] Figure 13 shows the distribution of the measured and predicted normalized streamwise unit discharge, $U_s h/(UH)$, which by definition has an average value of 1 in each cross-section. The rapid development of the transverse bed slope and its overshoot of the equilibrium value in the cross-section at 60° provoke a rapid spanwise redistribution of the discharge: in the cross-section at 60° more than 90% of the

discharge flows through the outer half of the cross-section and the maximum unit discharge is about three times higher than in the straight approach flow. The shallow inner half of the cross-section over the point bar is a kind of dead water zone. *Dietrich and Smith* [1983] and *Whiting and Dietrich* [1993] have called this important velocity redistribution induced by the bed topography "topographic steering". Downstream of the cross-section at 60°, more that 75% of the flow discharge is conveyed through the outer half of the cross-section. The spanwise distribution of streamwise unit discharge is modulated by the bed topography: its nonuniformity decreases from the cross-section at 60° to the one at 120°, and increases again toward the bend exit. In the straight outflow, flow tends to become uniform over the width. Note that the normalized unit streamwise discharge at the centerline remains about constant at 1, as postulated by *Odgaard* [1986, 1989].

[77] The model captures the major features of the (re)-distribution of $U_s h/(UH)$ in the simulation with a loose bed. However, predictions underestimate topographic steering by the point bar as well as the streamwise oscillations of $U_s h/(UH)$. Moreover, the model predicts a recirculation zone near the inner bank from the cross-section at 150° in the bend onto the cross-section P3.0 situated 3.0 m downstream
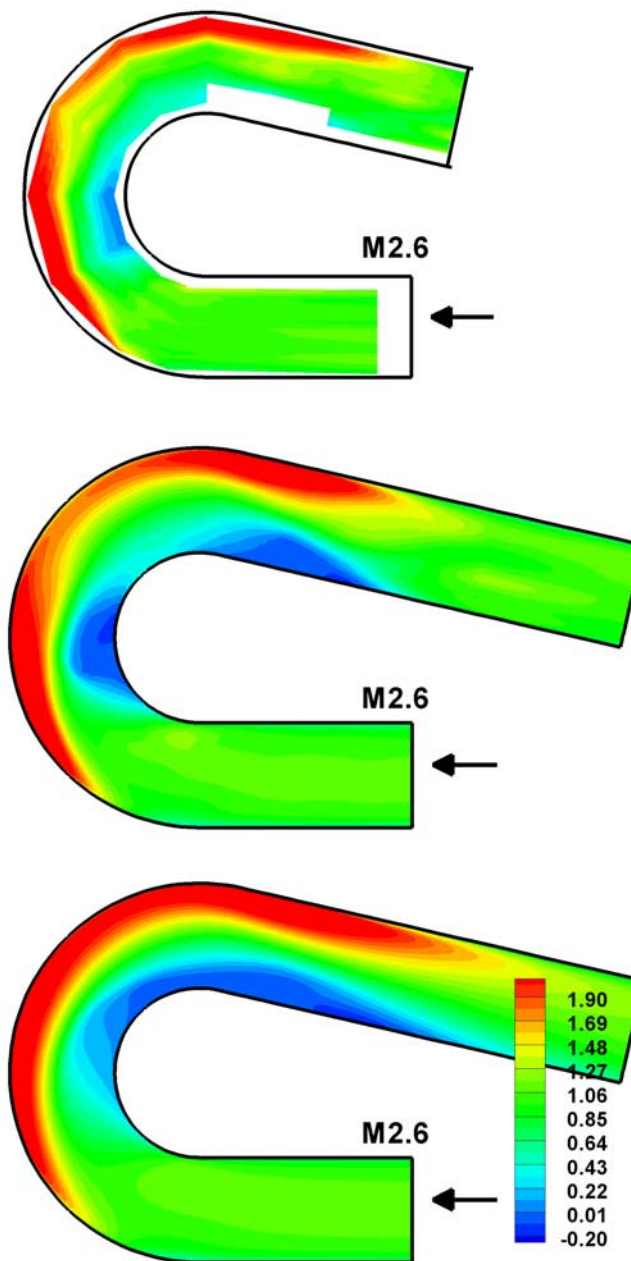
Figure 13. Distribution of the normalized streamwise unit discharge, $U_s h/(UH)$, in the bend with equilibrium bed. (a) Based on measurements (the shallowness of the flow near the inner bank just downstream of the bend exit did not allow flow measurements). (b) Predicted over the fixed prescribed measured bathymetry. (c) Predicted over the predicted bathymetry.

of the curved reach exit, which was not observed in the experiments. These differences may be attributed to differences between the measured and predicted bathymetry (see Figure 12).

[78] In order to confirm that differences between measured and predicted flow parameters can, to a large extent, be attributed to differences in the bathymetry, Figure 13b shows the predicted distribution of $U_s h/(UH)$ over the fixed prescribed measured bathymetry. Agreement with the measured distribution (Figure 13a) is much better than in

Figure 13c. The major remaining difference between measurements and predictions is the size and position of the regions of slowly moving flow over the shallow point bars. As mentioned before, these differences are not very relevant to the overall flow dynamics, since flow over the shallow part has negligible contribution to the discharge.

[79] Figure 13 indicates the dominant role of the bathymetry with respect to the distributions of the streamwise flow and unit discharge. This does not imply, however, that curvature induced cross-stream circulation is only a dominant process in a flat bed configuration but a negligible one in a mobile bed configuration. This is because it determines the direction of the bed shear stress and the sediment transport in the mobile bed case. The curvature induced cross-stream circulation cell induces an inward component of the bed shear stress that tends to move sediment inward and to build up a transverse bed slope. The equilibrium transverse bed slope is reached when the inward component of the bed shear stress is balanced by the outward gravitational pull on the sediment particles [e.g., *Engelund*, 1974; *Kikkawa et al.*, 1976; *Odgaard*, 1981]. Hence the cross-stream circulation indirectly determines the flow field by shaping the bathymetry.

[80] Figure 14 shows the distribution of the cross-stream circulation strength, parameterized by the normalized depth-averaged pseudo-streamfunction, $100\langle\psi\rangle/(UH)$. Cross-stream circulation is negligible in the shallow inner half of the cross-section and concentrated in the deep outer half of the cross-section. Similar to the flat bed experiment, cross-stream circulation increases toward a maximum value in the first part of the bend before decaying in the second part of the bend. The maximum measured value of $100\langle\psi\rangle/(UH) \approx 45$ is much higher than in the flat bed experiment. However, this is mainly to be attributed to the local increase in flow depth, h, which implicitly occurs in the definition of the pseudo-streamfunction ψ (see equations (13)−(15)). This dependence on h also explains why the evolution of $100\langle\psi\rangle/(UH)$ is strongly modulated by the bathymetry. The maximum value of $100\langle\psi\rangle/(UH) \approx 45$ is reached in the cross-section with maximum depth at $60°$. Subsequently, it decreases toward a value of $100\langle\psi\rangle/(UH) \approx 10$ at $120°$ and seems to increase slightly again toward the bend exit. The cross-stream circulation disappears gradually in the straight outflow reach. Contrary to the flat bed experiment, no counter-rotating outer bank cell of cross-stream circulation is observed in the equilibrium bed experiment.

[81] When simulating the flow field over the prescribed measured bathymetry, the model captures the position of the cell in the deepest part of the cross-section, as well as its increase upon entering the bend and the location of the maximum circulation strength. Moreover the model predicts the modulation of the circulation strength by the bed topography, as indicated by the increasing values around the bend exit. Similar to the flat bed configuration, the model seems to underpredict the cross-stream circulation in the flow region characterized by the highest values. When applying the model to predict the flow field and the bathymetry, discrepancies between the measurements and the predictions are amplified, although the principal characteristics of the cross-stream circulation pattern are still captured.

[82] Figures 15 and 16 show the measured and predicted profiles of the normalized streamwise and transverse veloc-
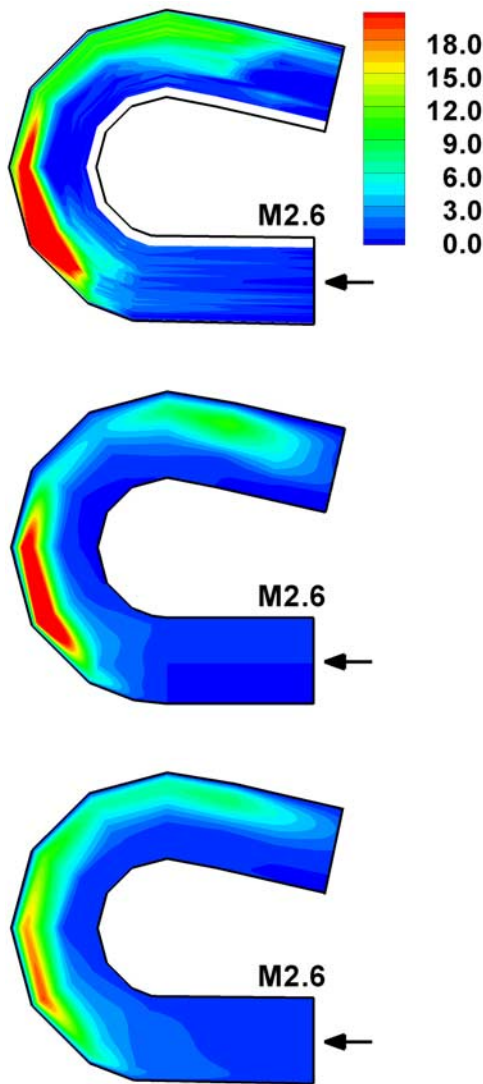
Figure 14. Distribution of the normalized depth-averaged cross-stream circulation strength, $100\langle\psi\rangle/(UH)$ in the bend with equilibrium bed. (top) Based on measurements (the shallowness of the flow near the inner bank just downstream of the bend exit did not allow flow measurements). (middle) Predicted over the fixed prescribed measured bathymetry. (bottom) Predicted over the predicted bathymetry. To facilitate comparison among the three cases, the maximum value of $100\langle\psi\rangle/(UH)$ was limited to 18 in the contour plots.

ities, v_s/U and v_n/U around the flume. The predicted profiles are computed over the prescribed measured equilibrium bathymetry. These figures allow gaining insight in the interaction between the complex 3D flow patterns and the bathymetry. Moreover, they allow further confirming that differences between measured and predicted flow parameters in Figures 13 and 14 can be largely attributed to differences between measured and predicted equilibrium bathymetries.

[83] Figure 15 shows that the measured and predicted v_s profiles increase monotonically from the bed toward the water surface in the cross-section at $30°$ in the bend. Further downstream in the bend, v_s profiles flatten significantly,

especially in the flow region occupied by the cross-stream circulation cell.

[84] Figure 16 shows that the distribution of the transverse velocity v_n is determined by two different flow processes: cross-flow represented by the depth-averaged transverse velocity, U_n, and cross-stream circulation parameterized by $v_n^* = v_n - U_n$. Contrary to the flat bed configuration, cross-stream circulation is concentrated over the deep outer part of the cross-section. Its maximum transverse velocities are of comparable magnitude to those in the flat bed experiment. Cross-flow is dominant over the shallow inner part of the cross-section. It is mainly driven by streamwise bathymetrical variations. The development of the transverse bed slope induced an outward cross-flow over the entire width in the cross-section at $30°$ in the bend. In the cross-section at $60°$, cross-stream circulation is established over the deep part, but topographic steering around the point bar induces very intense ($U_n/U \approx 0.5$) outward cross-flow in the inner half of the cross-section. In the cross-section at $120°$ downstream of the pronounced point bar, cross-flow in the inner part of the cross-section is oriented inward. The sudden flow accelerations/decelerations induced in the outer/inner half of the cross-section at the bend exit induce an outward cross-flow in the cross-section at $180°$. Finally, the recovery toward a straight channel flow velocity distribution in the outflow reach is accompanied by inward cross-flow. Although significant quantitative differences exist between measurements and predictions, the model captures the major features of the v_n distribution. These differences are also expected to affect the accuracy of the predictions of the angle θ_b in the model used to account for gravitational bed slope effects (equation (11)).

[85] Figure 17 focuses on the measured and predicted patterns of the streamwise velocity, cross-stream circulation, and streamwise vorticity in the cross-section at $90°$.

[86] The curvature induced cross-stream circulation cell is concentrated over the deepest part of the cross-section, where it determines the v_s-pattern. Imagine a virtual situation over the deepest part of the cross-section where the cross-stream circulation cell is situated, with "straight channel flow" v_s-profiles that increase monotonically from the bed toward the water surface. Advective momentum transport by the cross-stream circulation cell would shift the low near-bed velocities toward the water surface and the high near-surface velocities toward the bed in clockwise sense, resulting in the measured v_s-pattern. The core of maximum velocities is found near the bed and the v_s profiles decrease toward the water surface. Contrary to flat bed case, no counter-rotating outer bank cell of cross-stream circulation is measured in the equilibrium bed configuration.

[87] When simulating the flow over the fixed prescribed equilibrium bathymetry, the model reproduces accurately the main features of the streamwise and cross-stream flow as well as their interaction in the cross-section at $90°$ (Figure 17), although the strength of the cross-stream circulation cell as shown by the ψ contours is somewhat underpredicted. This is consistent with observations concerning the pattern of the depth-averaged strength of the cross-stream circulation around the bend (see Figure 14). In line with the foregoing results, discrepancies between the measured and predicted flow fields increase when also the equilibrium
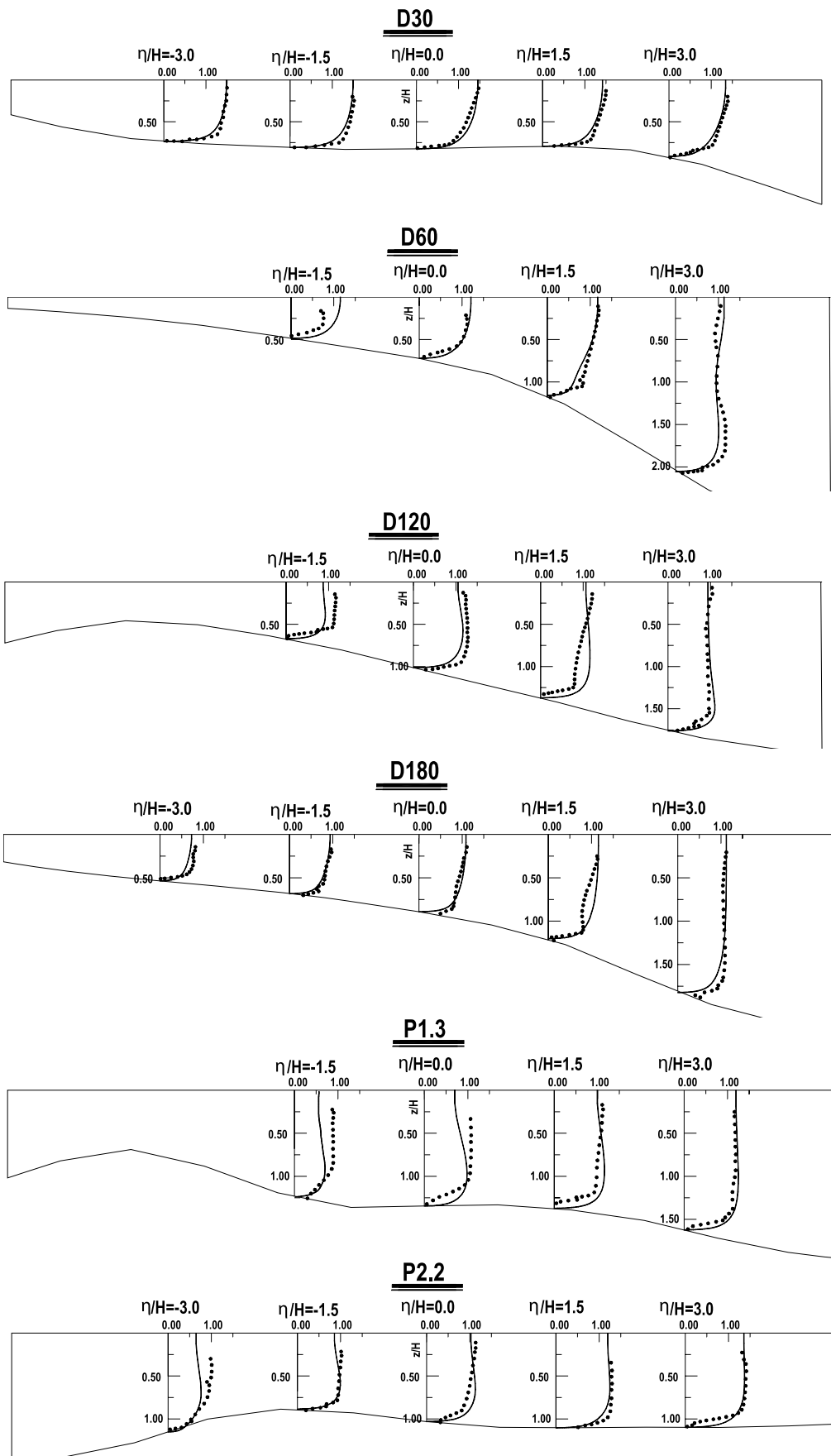
Figure 15. Comparison between measured (symbols) and predicted (solid lines) vertical profiles of the normalized streamwise velocity, v_s/U, in several cross-sections along the bend with equilibrium bed.
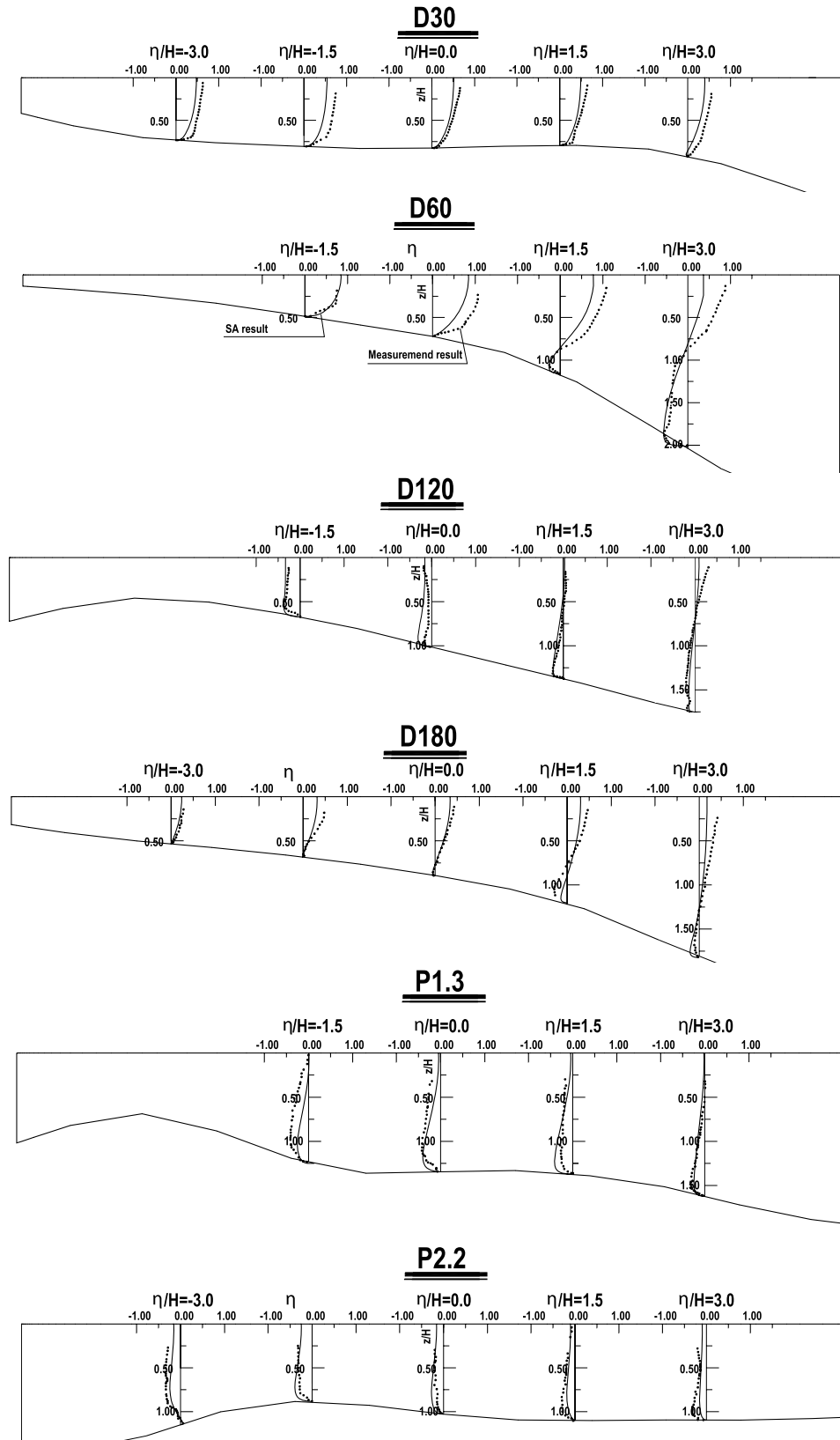
Figure 16. Comparison between measured (symbols) and predicted (solid lines) vertical profiles of the normalized transverse velocity, v_n/U, in several cross-sections along the bend with equilibrium bed.
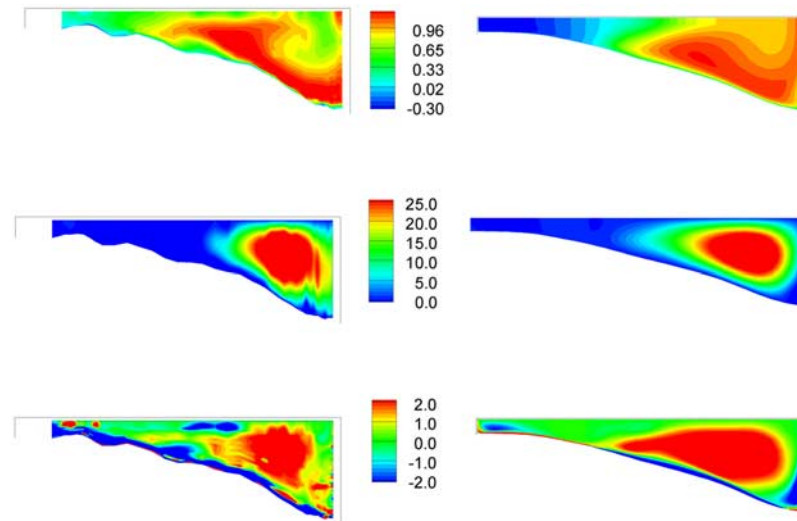
Figure 17. Patterns of the (top) normalized streamwise velocity v_s/U, (middle) normalized cross-stream circulation $100\psi/(UH)$, and (bottom) streamwise vorticity $\omega_s(H/U)$ in the cross-section at $90°$ in the bend with equilibrium bed. Comparison between (left) measurements and (right) predictions over the fixed prescribed measured equilibrium bathymetry.

bathymetry is predicted by the model, although the main flow features are still satisfactorily captured (not shown). The level of agreement shown by the streamwise vorticity contours is similar to the one observed for the ψ contours. The patch of relatively high positive vorticity induced by the cross-stream flow motions is confined to the half section on the outer-wall side.

[88] Figure 18 shows the distributions of the streamwise velocity and streamwise vorticity in the cross-section at $180°$ obtained from experiment and the simulation with a prescribed measured equilibrium bathymetry. In this section the core of the region characterized by relatively large values of the streamwise velocity switches back to the free surface. Its center is situated close to the middle of the section, slightly on the outer bank side. The core appears to be slightly more compact and to extend at deeper levels below the free surface in the simulation. The streamwise vorticity distributions are also qualitatively similar. An elongated region of relatively high positive vorticity is observed in the near-bed region over most of the section.

In both experiment and simulation, the largest amplification of the positive vorticity is observed to occur in the shallower part of the section. Still, the local amplification of vorticity inside this patch is somewhat different in experiment and simulation. It is not clear if a significant part of these differences are due to errors related to estimating velocity gradients from velocity measurements conducted on a fairly coarse measurement mesh.

[89] Figure 19 shows the distribution of the normalized depth-averaged turbulent kinetic energy, $\langle k \rangle/(1/2u_*^2)$. It remains about constant from the straight approach reach onto the cross section at $60°$ in the bend. A core of high turbulent kinetic energy develops downstream of the cross-section at $60°$. The core switches toward the outer side such that it is found in the region between the centerline and $\eta \approx 2.5H$ downstream of the cross-section at $120°$. Values in this core increase onto the bend exit and reach a maximum that is about four times higher than in the straight approach flow. Interestingly, the flow region between the outer bank and the core of high turbulence activity is characterized by
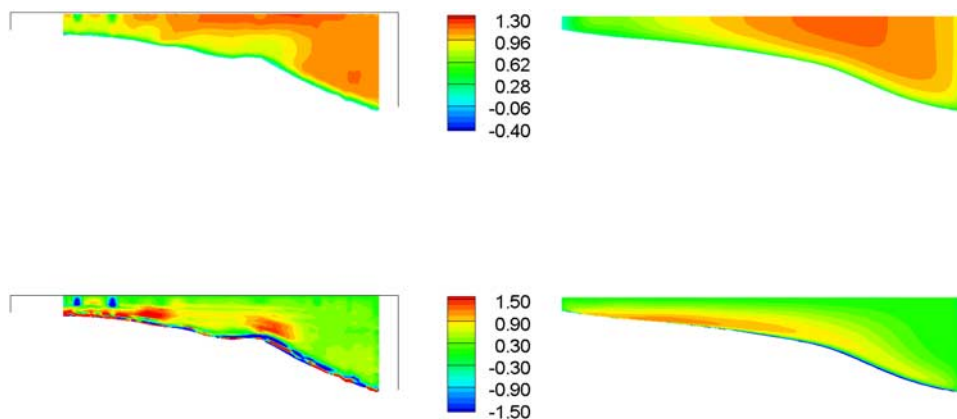

Figure 18. Patterns of the (top) normalized streamwise velocity v_s/U and (bottom) streamwise vorticity $\omega_s(H/U)$ in the cross-section at $180°$ in the bend with equilibrium bed. Comparison between (left) measurements and (right) predictions over the fixed prescribed measured equilibrium bathymetry.
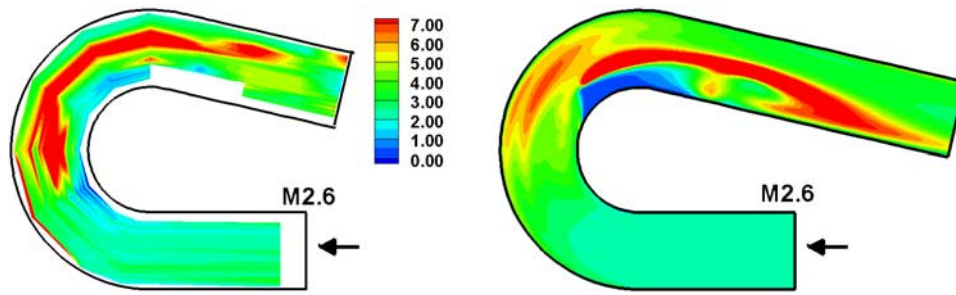
Figure 19. Distribution of the normalized depth-averaged turbulent kinetic energy, $\langle k \rangle / (1/2 u_*^2)$ in the bend with equilibrium bed. (left) Based on measurements (the shallowness of the flow near the inner bank just downstream of the bend exit did not allow flow measurements). (right) Predicted.

values that are hardly higher than in the straight approach flow. Recovery toward a straight channel flow turbulence activity in the outflow reach is slower than in the flat bed configuration.

[90] The mechanisms underlying the increase of turbulence activity differ from the flat bed case, where they were directly related to additional straining by the cross-stream circulation. We postulate that the core of high turbulence activity over the equilibrium bed is mainly due to the formation of a relatively strong shear layer between the low-velocity flow over the shallow inner part of the cross-section and the high velocity flow over the deep part of the cross-section (see Figure 13).

[91] The predicted distribution of $\langle k \rangle / (1/2 u_*^2)$ increases gradually from the bend entry onto the cross-section at $120°$, where maximum values are reached in the outer half of the cross-section that are about three times higher than in the straight approach. Subsequently, they remain about constant until the cross-section at $160°$ before starting decaying rapidly. From the cross-section at $150°$ on, a core of high turbulent activity is predicted inward from the centerline at the edge of the predicted recirculation zone (see Figure 13). This core is attributed to the shear layer between the low velocities in the recirculation zone and the high velocities in the deep part of the cross-section. Although differences between the measured and predicted patterns are significant, the model captures the essential mechanisms that lead to the generation of turbulence activity.

6. Discussion

[92] The validated 3D morphodynamic model can provide quantities that are difficult to measure directly in the laboratory or the field. Figure 20, for example, shows the distribution of the predicted normalized bed shear stress, $\tau_b / (\rho U^2)$, in the flat and equilibrium bed configurations. In the flat bed case, the maximum bed shear stress induced by curvature effects is about twice as high as the bed shear stress in the straight inflow reach. The ratio is even higher in the equilibrium bed case. The corresponding sediment transport in the flat bed case would be about three times higher than in the straight inflow according to most formulae that predict sediment transport to be roughly proportional to the bed shear stress to the power 1.5. The distribution of the bed shear stress around the bend is fundamentally different for the two cases, however. For the flat bed case, the maximum bed shear stress occurs at the inner side of the bend just downstream of the bend entry. The core of maximum bed shear stress shift gradually outward around the bend, and a core of high values forms at the outer bank just downstream of the bend exit. Over the equilibrium bed topography, relatively high values of the bed shear stress are predicted over the point bar at the inner bank just downstream of the bend entry. This point bar shifts the core of maximum bed shear stress toward the outer part of the cross-section. High values of the bed shear stress are thus mainly located in the deepest parts of the cross-sections, starting with the cross-section at $60°$. Note that the regions of high/low bed shear stress over the flat bed do not correspond to scoured/deposited regions in the equilibrium bed configuration. This observation highlights the strong nonlinear character of the interaction between the complex 3D flow, the sediment transport and the bathymetry.

[93] The curvature induced increase of the bed shear stress can be attributed to three phenomena. First, the velocity redistribution is accompanied by a bed shear stress redistribution, since $\tau_b \sim U_s^2$. Second, the cross-stream circulation induces a relatively high cross-stream velocity
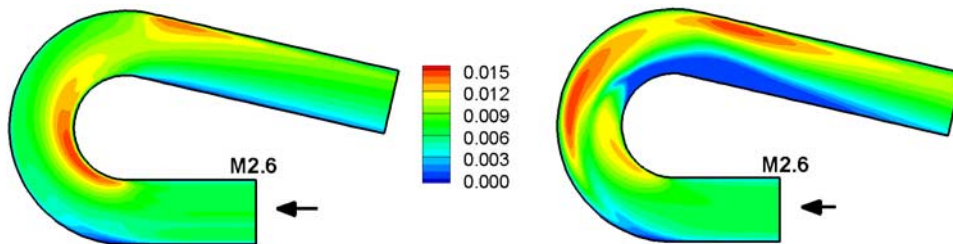

Figure 20. Distribution of the normalized shear stress on the bed, $\tau_b / (\rho U^2)$. (left) Flat bed. (right) Equilibrium bed.
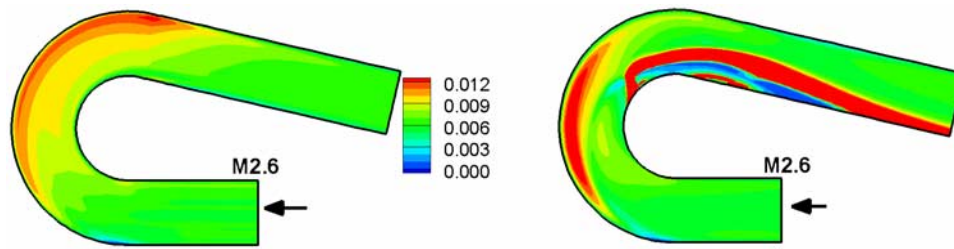
Figure 21. Distribution of the Chézy type friction coefficient, $C_f = \tau_b/(\rho U_s^2)$. (left) Flat bed. (right) Equilibrium bed.

component close to the bed that generates an additional cross-stream component of the bed shear stress. It is this component that determines the transverse equilibrium bed slope. Third, the flattening of the v_s-profiles gives rise to an increase of the near bed velocity gradient, $\partial v_s/\partial z$, and an amplification of the bed shear stress. Figure 20 shows that regions of high bed shear stress correspond to regions of high cross-stream circulation (Figures 3, 8, 14, and 17) with pronounced flattening of v_s-profiles.

[94] The latter two phenomena influence the relation between the bed shear stress, τ_b, and the local depth-averaged streamwise velocity, U_s, which has to be prescribed in depth-averaged flow models, for example in the form of the Chézy type friction coefficient $C_f = \tau_b/\rho U_s^2$. Figure 21 shows the predicted distributions of C_f in the flat and equilibrium bed configurations. The flume-averaged value estimated from the experiments is $C_f = 0.0086$ for the flat bed configuration and $C_f = 0.0100$ for the equilibrium bed configuration, indicating that total energy losses are slightly higher in the equilibrium bed configuration. Interestingly, zones of amplified bed shear stress (see Figure 20) do not always correspond to zones with increased C_f coefficient, that are mainly predicted in the deepest part of the cross-section in both configurations. In these regions the maximum amplification of C_f with respect to the value in the straight inflow is of the order of 50%. Notice that an underestimation of the bed shear stress by 50%, for example by a 2D model with constant C_f, would lead to an underestimation of the sediment transport by about 100% (the sediment transport rate is about proportional to the bed shear stress to the power 1.5 according to most models), which would have a significant influence on bathymetry predictions. The zone of very high C_f values predicted in the inner half of the cross-section in the equilibrium bed configuration is related to the presence of very low speed flow and flow recirculation ($C_f \sim U_s^{-2}$).

7. Concluding Remarks

[95] The present paper focused on two configurations in very sharp open-channel bends: a first configuration with flat bed represents the initial phase of the scouring/deposition process in open-channel bends, whereas a second configuration represents the equilibrium bathymetry in the final phase.

[96] The paper presented detailed experimental data on the bathymetry and the flow field for both configurations, including depth-averaged distributions of the streamwise velocity, the cross-stream circulation and the turbulent kinetic energy, the evolution of the profiles of streamwise

and transverse velocity around the bend, and 3D patterns of streamwise velocity, cross-stream circulation and/or streamwise vorticity and turbulent kinetic energy in the cross-section at 90° where the cross-stream circulation is the strongest and in the cross-section at 180°.

[97] A fully 3D nonhydrostatic RANS model for flow, sediment transport and bathymetry with near-wall modeling capabilities was evaluated by means of the experiments. In flow simulations over a fixed bathymetry, the model simulates accurately the main characteristics of the complex 3D flow field, including processes such as the interaction between the deformation of the v_s-profiles and the strength of the cross-stream circulation cells, the production of turbulent kinetic energy, etc. The errors were found to be larger for the transverse velocity profiles compared to the streamwise profiles. When simulating the interaction between the flow field and the mobile bed, deviations between model predictions and measurements increased, but the main features were still captured by the model. In the light of the complex nonlinear interaction between the main flow, the cross-stream flow and the mobile bed, and by comparison with similar predictions of flow and morphodynamics changes in bends of lower curvature available in the literature, the obtained accuracy and predictive capacity of the model can be considered satisfactory.

[98] The experimental data and numerical simulations testify of the complex nonlinear interaction between the downstream velocity and the cross-stream circulation. This interaction is further complicated by interaction with the bathymetry, which leaves a strong fingerprint on all characteristics of the flow field. These experimental data enhanced our insight in fluvial processes in sharp open-channel bends, and indicated significant differences in the distribution of the streamwise vorticity, turbulent kinetic energy and transverse velocity between configurations with flat and equilibrium bathymetry. Hence results obtained in laboratory flumes over a flat bathymetry may not be representative or relevant for natural river configurations.

[99] The present study allowed to better understand to what extent uncertainties (discrepancies between measurements and predictions) have to be attributed to the flow module of the morphodynamic code and to what extent they are due to the modeling of the sediment transport which determines the evolution of the bed. In our opinion this is an important question, as depending on the answer future efforts should be directed toward using more complex sediment transport (in particular, bed-load transport) models or more complex turbulence models (e.g., Reynolds stress models, hybrid RANS-LES approaches, or LES with wall functions). The results in the present paper make the case

that both directions are worth pursuing in order to alleviate the weaknesses of present numerical models for prediction of flow, sediment transport and morphodynamics in alluvial bends and river reaches.

[100] The main discrepancies between the model predictions and the measurements occur in the flow region near the outer bank: the model cannot resolve the observed outer bank cell of cross-stream circulation measured in the flat bed experiment, while significant differences between measurements and predictions are observed for the turbulent kinetic energy in the equilibrium experiment. According to *Blanckaert and de Vriend* [2004, 2005a, 2005b], the simulation of both processes requires turbulence models that resolve turbulence anisotropy and the kinetic energy transfer between mean flow and turbulence.

[101] In the discussion on the predictive capabilities of the numerical model, it should be accentuated that the test experiments were designed to exaggerate, hence make better visible, curvature related processes, leading to configurations that are extremely severe for numerical models and not very representative of natural river conditions. Natural rivers typically have more moderately curved bends, never have curvature discontinuities but gradually varying curvature and are characterized by inclined channel banks.

[102] The range of application of the 3D morphodynamic model in its present form is mainly situated on the local scale, for river reaches with a length of the order of 100 times the flow width. The parallelization of the code is expected to enhance by at least one order of magnitude the domain sizes that can be simulated and to make time-accurate simulations feasible.

References

Batchelor, G. K. (1967), *An Introduction to Fluid Dynamics*, Cambridge Univ. Press, New York.

Bathurst, J. C., C. R. Thorne, and R. D. Hey (1979), Secondary flow and shear stress at river bends, *J. Hydraul. Div., Am. Soc. Civ. Eng.*, *105*, 1277–1295.

Blanckaert, K. (2001), Discussion on: Bend-flow simulation using 2D depth-averaged model, by H. C. Lien et al., *J. Hydraul. Eng., Am. Soc. Civ. Eng.*, *127*(2), 167–170.

Blanckaert, K. (2002), Flow and turbulence in sharp open-channel bends, Ph.D. thesis Nr 2545, Ecole Polytechnique Fédérale Lausanne, Switzerland. (Available at ftp://lrhmac15.epfl.ch/Pub/Thesis/Blanckaert/PhD)

Blanckaert, K., F. Buschman, R. Schielen, and J. H. A. Wijbenga (2008), Redistribution of velocity and bed shear stress in straight and curved open channels by means of a bubble screen. Laboratory experiments, *J. Hydraul. Eng., Am. Soc. Civ. Eng.*, *134*(2), 184–195, doi:10.1061/(ASCE)0733-9429(2008)134:2(184).

Blanckaert, K., and H. J. de Vriend (2003), Non-linear modeling of mean flow redistribution in curved open channels, *Water Resour. Res.*, *39*(12), 1375, doi:10.1029/2003WR002068.

Blanckaert, K., and H. J. de Vriend (2004), Secondary flow in sharp open-channel bends, *J. Fluid Mech.*, *498*, 353–380, doi:10.1017/S0022112003006979.

Blanckaert, K., and H. J. de Vriend (2005a), Turbulence characteristics in sharp open-channel bends, *Phys. Fluids, AIP*, *17*(5), 055102, doi:10.1063/1.1886726.

Blanckaert, K., and H. J. de Vriend (2005b), Turbulence structure in sharp open-channel bends, *J. Fluid Mech.*, *536*, 27–48.

Blanckaert, K., and W. H. Graf (2001), Mean flow and turbulence in open-channel bend, *J. Hydraul. Eng., Am. Soc. Civ. Eng.*, *127*(10), 835–847.

Blanckaert, K., and W. H. Graf (2004), Momentum transport in sharp open-channel bends, *J. Hydraul. Eng., Am. Soc. Civ. Eng.*, *130*(3), 186–198, doi:10.1061/(ASCE)0733-9429(2004)130:3(186).

Blanckaert, K., and U. Lemmin (2006), Means of noise reduction in acoustic turbulence measurements, *J. Hydraul. Res., IAHR*, *44*(1), 3–17.

Blanckaert, K., L. Glasson, H. R. A. Jagers, and C. J. Sloff (2003), Quasi-3D simulation of flow in sharp open-channel bends with horizontal and developed bed topography, in *Proc. Int. Symp. Shallow Flows*, vol. I, edited by G. Jirka and W. Uijttewall, pp. 93–100, Techn. Univ. Delft, Delft, Netherlands.

Celik, I., and W. Rodi (1988), Modeling of suspended sediment transport in non-equilibrium situations, *J. Hydraul. Eng., Am. Soc. Civ. Eng.*, *114*(10), 1157–1191.

Choi, S. U., T. B. Kim, and K. D. Min (2005), 2D finite element modeling of bed elevation change in a curved channel, in *River, Coastal and Estuarine Morphodynamics Conference*, edited by M. Garcia and G. Parker, pp. 350–356, The University of Illinois, Urbana Champaign, Illinois.

Constantinescu, S. G., and K. Squires (2004), Numerical investigation of flow over sphere in the subcritical and supercritical regimes, *Phys. Fluids*, *16*(5), 1446–1465.

Darby, S. E., A. M. Alabyan, and M. J. Van de Wiel (2002), Numerical simulation of bank erosion and channel migration in meandering rivers, *Water Resour. Res.*, *38*(9), 1163, doi:10.1029/2001WR000602.

de Vriend, H. J. (1981a), Velocity redistribution in curved rectangle channels, *J. Fluid Mech.*, *107*(6), 423–439.

de Vriend, H. J. (1981b), Steady flow in shallow channel bends, Report No. 81-3, Lab. Fl. Mech., Dept. Civ. Eng., Delft Univ. Techn., Delft, The Netherlands.

de Vriend, H. J., and H. J. Geldof (1983), Main flow velocity in short and sharply curved river bends, Report No. 83-6, Lab. Fl. Mech., Dept. Civ. Eng., Delft Univ. Techn., Delft, Netherlands.

de Vriend, H. J., and N. Struiksma (1984), Flow and bed deformation in river bends, in *River Meandering*, edited by C. M. Elliot, pp. 810–828, ASCE, New York.

Dietrich, W. E., and J. D. Smith (1983), Influence of the point bar on flow through curved channels, *Water Resour. Res.*, *19*(5), 1173–1192.

Engelund, F. (1974), Flow and bed topography in channel bends, *J. Hydraul. Div., Am. Soc. Civ. Eng.*, *100*(11), 1631–1648.

Engelund, F., and E. Hansen (1967), *A Monograph on Sediment Transport in Alluvial Streams*, Teknisk Vorlag, Copenhagen, Denmark.

Finnie, J., B. Donnell, J. Letter, and R. S. Bernard (1999), Secondary flow correction for depth-averaged flow calculations, *J. Eng. Mech., Am. Soc. Civ. Eng.*, *125*(7), 848–863.

Ghamry, H. K. (1999), Two dimensional vertically averaged and momentum equations for shallow free surface flows, Ph.D. thesis, University of Alberta, Edmonton Alta., Canada.

Ghamry, H. K., and P. M. Steffler (2005), 2D depth-averaged modeling of flow in curved open channels, *J. Hydraul. Res., IAHR*, *43*(1), 44–55.

Henderson, F. M. (1966), *Open Channel Flows*, Macmillan Company, New York.

Hurther, D., and U. Lemmin (1998), A constant beamwidth transducer for three-dimensional Doppler profile measurements in open channel flow, *Meas. Sci. Technol., IOP*, *9*(10), 1706–1714.

Jin, Y. C., and P. M. Steffler (1993), Predicting flow in open curved channels by depth-averaged method, *J. Hydraul. Eng., Am. Soc. Civ. Eng.*, *119*(1), 109–124.

Johannesson, H., and G. Parker (1989), Velocity redistribution in meandering rivers, *J. Hydraul. Eng.*, *115*(8), 1019–1039.

Kassem, A. A., and M. H. Chaudhry (2002), Numerical modeling of bed evolution in channel bends, *J. Hydraul. Eng., Am. Soc. Civ. Eng.*, *128*(5), 507–514.

Kikkawa, H., S. Ikeda, and A. Kitagawa (1976), Flow and bed topography in curved open channels, *J. Hydraul. Div., Am. Soc. Civ. Eng.*, *102*(9), 1327–1342.

Khosronejad, A., C. Rennie, S. Neyshabouri, and R. D. Townsend (2007), 3D numerical modeling of flow and sediment transport in laboratory channel bends, *J. Hydraul. Eng.*, *133*(10), 1123–1134.

Lemmin, U., and T. Rolland (1997), Acoustic velocity profiler for laboratory and field studies, *J. Hydraul. Eng., Am. Soc. Civ. Eng.*, *123*(12), 1089–1098.

Menter, F. R. (1994), Two-equation eddy-viscosity turbulence models for engineering applications, *AIAA J.*, *32*(8), 1598–1605.

Minh Duc, B., Th. Wenka, and W. Rodi (2004), Numerical modelling of bed deformation in laboratory channels, *J. Hydraul. Eng., Am. Soc. Civ. Eng.*, *130*(9), 894–904.

Odgaard, A. J. (1981), Transverse bed slope in alluvial channel bends, *J. Hydraul. Div., Am. Soc. Civ. Eng.*, *107*(12), 1677–1694.

Odgaard, A. J. (1986), Meander flow model. I: Development, *J. Hydraul. Eng., Am. Soc. Civ. Eng.*, *112*(12), 1117–1136.

Odgaard, A. J. (1989), River meander model. I: Development, *J. Hydraul. Eng., Am. Soc. Civ. Eng.*, *115*(11), 1433–1450.

Odgaard, A. J., and M. A. Bergs (1988), Flow processes in a curved alluvial channel, *Water Resour. Res.*, *24*, 45–56.

Olesen, K. W. (1985), Experiments with graded sediment in the DHL curved flume, *Report R 657-XXII M1771*, Delft Hydr. Lab., Delft, Netherlands.

Rozovskii, I. L. (1957), *Flow of Water in Bends of Open Channels*, Acad. of Sci. of the Ukr., Kiev. (English translation, Isr. Program for Sci. Transl., Jerusalem, 1961.)

Ruther, N., and N. R. Olsen (2005), 3D modeling of sediment transport in a narrow 90° channel bend, *J. Hydraul. Eng., Am. Soc. Civ. Eng.*, *131*(10), 917–920.

Ruther, N., and N. R. Olsen (2006), 3D modeling of transient bed deformation in a sine-generated laboratory channel with two different width to depth ratios, Proceedings of River Flow 2006 Conference, Lisbon, Portugal.

Sekine, M., and G. Parker (1992), Bed load transport on transverse slope, *J. Hydraul. Eng., Am. Soc. Civ. Eng.*, *118*(4), 513–535.

Shimizu, Y., and T. Itakura (1989), Calculation of bed variation in alluvial channels, *J. Hydraul. Div., Am. Soc. Civ. Eng.*, *115*(3), 367–384.

Shimizu, Y., H. Yamaguchi, and T. Itakura (1990), Three-dimensional computation of flow and bed deformation, *J. Hydraul. Eng., Am. Soc. Civ. Eng.*, *116*(9), 1090–1108.

Spalart, P. R. (2000), Trends in turbulence treatments, AIAA Paper 2000–2306, Fluids 2000, Denver.

Struiksma, N. (1983), Point bar initiation in bends of alluvial rivers with dominant bed transport, *TOW Report R657-XVII/W308-III*, Delft Hydr. Lab., Delft, Netherlands.

Struiksma, N., K. W. Olesen, C. Flokstra, and H. J. de Vriend (1985), Bed deformation in curved alluvial channels, *J. Hydraul. Res., IAHR*, *23*(1), 57–79.

van Rijn, L. C. (1984), Sediment transport. part I: Bed load transport, *J. Hydraul. Eng., Am. Soc. Civ. Eng.*, *110*(10), 1431–1456.

Vasquez, J. A., R. G. Millar, and P. M. Steffler (2005), Vertically-averaged and momentum model for alluvial bend morphology, in *River, Coastal and Estuarine Morphodynamics Conference*, edited by M. Garcia and G. Parker, pp. 445–453, The Univ. of Illinois, Urbana Champaign, Illinois.

Whiting, P. J., and W. E. Dietrich (1993), Experimental studies of bed topography and flow patterns in large amplitude meanders. 2: Mechanisms, *Water Resour. Res.*, *29*(11), 3615–3622.

Wilcox, W. C. (1993), *Turbulence Modeling for CFD*, DCW Industries, Inc., LA Canada, Canada.

Wu, W. (2004), Depth-averaged 2-D numerical modeling of unsteady flow and nonuniform sediment transport in open channels, *J. Hydraul. Eng., Am. Soc. Civ. Eng.*, *130*(10), 1013–1024.

Wu, W., W. Rodi, and T. Wenka (2000), 3D numerical modeling of flow and sediment transport in open channels, *J. Hydraul. Eng., Am. Soc. Civ. Eng.*, *126*(1), 4–15.

Yeh, K. C., and J. F. Kennedy (1993), Moment model of non uniform channel bend flow. II: Erodible beds, *J. Hydraul. Eng., Am. Soc. Civ. Eng.*, *119*(7), 796–815.

Yen, C. L. (1967), Bed configuration and characteristics of subcritical flow in a meandering channel, Ph.D. thesis, The Univ. of Iowa, Iowa City, Iowa.

Zeng, J. (2006), Fully 3D non-hydrostatic model to compute flow, sediment transport and bed morphology changes for alluvial open channel bends, Ph.D. thesis, The Univ. of Iowa, Iowa City, Iowa.

Zeng, J., S. G. Constantinescu, and L. Weber (2005a), A fully 3D non-hydrostatic models for prediction of flow, sediment transport and bed morphology in open channels, in *XXXIst International Association Hydraulic Research Congress*, edited by B.-H. Jun et al., pp. 554–560, IAHR, Seoul, Korea.

Zeng, J., S. G. Constantinescu, and L. Weber (2005b), Validation of a computational model to predict suspended and bed load sediment transport and equilibrium bed morphology in open channels, in *River, Coastal and Estuarine Morphodynamics Conference*, edited by M. Garcia and G. Parker, pp. 829–836, Univ. of Illinois, Urbana Champaign, Ill., October 2005.

Zeng, J., S. G. Constantinescu, and L. Weber (2008), A 3D non-hydrostatic model to predict flow and sediment transport in loose bed channel bends, *J. Hydraul. Res.*, *46*(3), 356–372, doi:10.3826/jhr.2008.3328.

K. Blanckaert, Faculty of Civil Engineering and Geosciences, Delft University of Technology, Stevinweg 1, P.O. Box 5048, 2628 CN, Delft, Netherlands. (koen.blanckaert@epfl.ch)

G. Constantinescu and L. Weber, Department of Civil and Environmental Engineering, IIHR-Hydroscience and Engineering, University of Iowa, 100 Maxwell Stanley Hydraulics Laboratory, Iowa City, IA 52242, USA. (sconstan@engineering.uiowa.edu; lweber@uiowa.edu)

J. Zeng, Operation and Hydro Data Management Division, South Florida Water Management District, 3301 Gun Club Road, MSC 5736, West Palm Beach, FL 33406, USA. (jzeng@sfwmd.gov)